

Glucose controls lipolysis through Golgi PtdIns4P-mediated regulation of ATGL

Received: 1 June 2023

Accepted: 23 February 2024

Published online: 1 April 2024

 Check for updates

Lianggong Ding¹, Florian Huwyler², Fen Long¹, Wu Yang³, Jonas Binz², Kendra Wernlé^{4,7}, Matthias Pfister^{4,7}, Manuel Klug¹, Miroslav Balaz⁵, Barbara Ukropcova⁵, Jozef Ukropec⁵, Chunyan Wu¹, Tongtong Wang¹, Min Gao^{1,6}, Pierre-Alain Clavien^{4,7}, Philipp Dutkowski⁴, Mark W. Tibbitt^{2,7} & Christian Wolfrum¹✉

Metabolic crosstalk of the major nutrients glucose, amino acids and fatty acids (FAs) ensures systemic metabolic homeostasis. The coordination between the supply of glucose and FAs to meet various physiological demands is especially important as improper nutrient levels lead to metabolic disorders, such as diabetes and metabolic dysfunction-associated steatohepatitis (MASH). In response to the oscillations in blood glucose levels, lipolysis is thought to be mainly regulated hormonally to control FA liberation from lipid droplets by insulin, catecholamine and glucagon. However, whether general cell-intrinsic mechanisms exist to directly modulate lipolysis via glucose sensing remains largely unknown. Here we report the identification of such an intrinsic mechanism, which involves Golgi PtdIns4P-mediated regulation of adipose triglyceride lipase (ATGL)-driven lipolysis via intracellular glucose sensing. Mechanistically, depletion of intracellular glucose results in lower Golgi PtdIns4P levels, and thus reduced assembly of the E3 ligase complex CUL7^{FBXWS} in the Golgi apparatus. Decreased levels of the E3 ligase complex lead to reduced polyubiquitylation of ATGL in the Golgi and enhancement of ATGL-driven lipolysis. This cell-intrinsic mechanism regulates both the pool of intracellular FAs and their extracellular release to meet physiological demands during fasting and glucose deprivation. Moreover, genetic and pharmacological manipulation of the Golgi PtdIns4P–CUL7^{FBXWS}–ATGL axis in mouse models of simple hepatic steatosis and MASH, as well as during ex vivo perfusion of a human steatotic liver graft leads to the amelioration of steatosis, suggesting that this pathway might be a promising target for metabolic dysfunction-associated steatotic liver disease and possibly MASH.

The catabolism of glucose, amino acids and fatty acids (FAs) is a central function of almost all cell types to maintain energy requirements for their various cellular activities. FAs have the highest energy density and most are esterified into triglycerides (TGs) and stored in lipid droplets (LDs) to avoid toxicity¹. During starvation, LDs are mobilized to liberate FAs for satisfying cellular energy demands via lipolysis or autophagic

degradation of LDs (that is, lipophagy)^{1–3}. Lipolysis is executed sequentially by adipose triglyceride lipase (ATGL), hormone-sensitive lipase (HSL) and monoacylglycerol lipase (MGL), while lipophagy is dependent on lysosomal acid lipase^{1,4,5}. Although LDs can form in almost any cell types, adipose tissue has the highest LD abundance. In the presence of an adequate glucose supply, insulin signalling increases lipogenesis while

A full list of affiliations appears at the end of the paper. ✉ e-mail: christian-wolfrum@ethz.ch

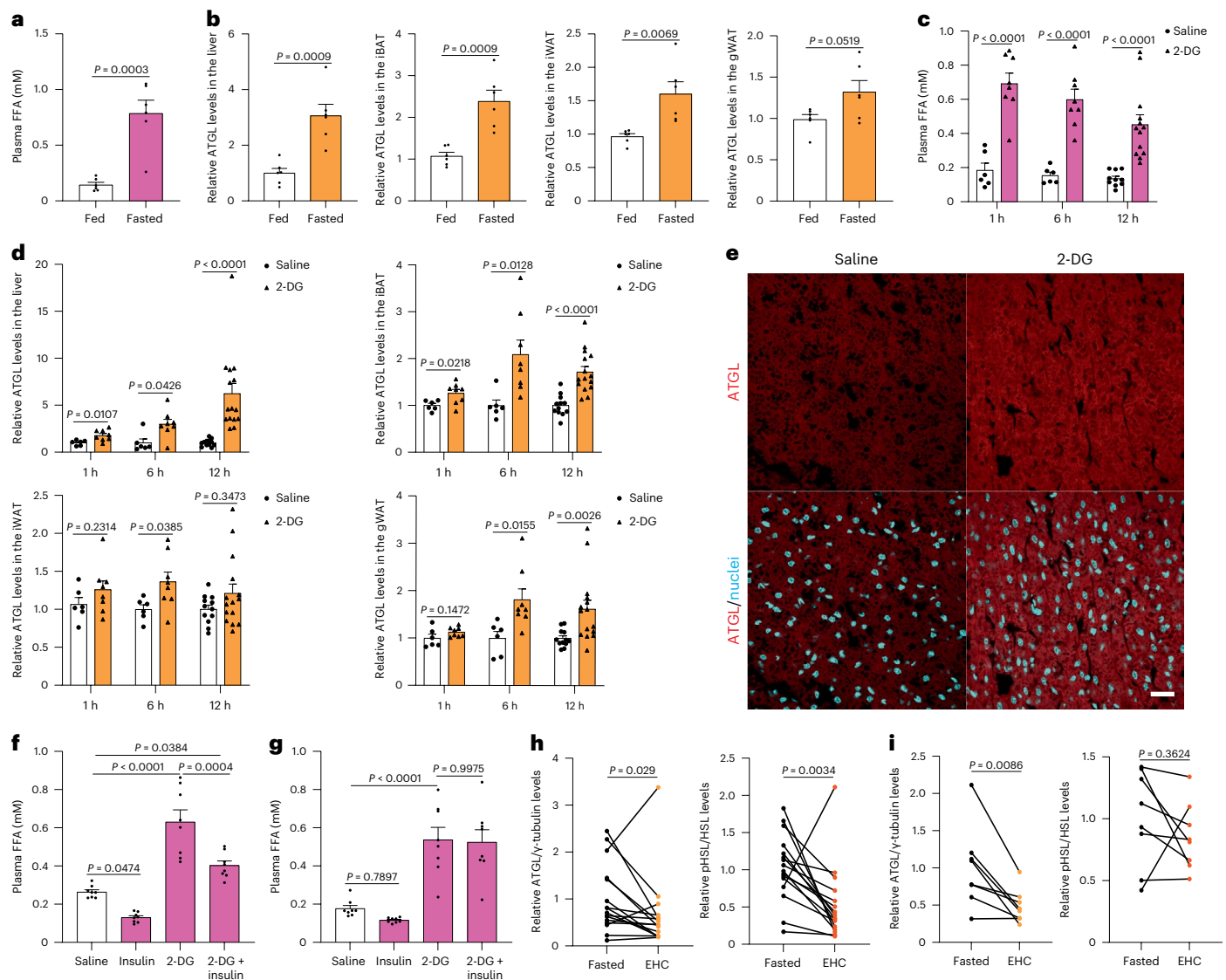


Fig. 1 | Glucose deprivation increases lipolysis via ATGL stabilization in the adipose depots and liver. **a,b**, Quantification of plasma FFA levels (**a**) and ATGL levels (**b**) in the liver and adipose depots after 24 h fasting ($n = 6$ mice per group). **c**, Plasma FFA levels in the mice 1 h, 6 h and 12 h after 2-DG ($2 \text{ g kg}^{-1} \text{ BW}$) administration (1 h and 6 h, $n = 6$ mice for saline and 8 mice for 2-DG group; 12 h, $n = 10$ mice for saline and 13 mice for 2-DG group). **d**, Quantification of ATGL levels in the liver and adipose depots collected 1 h, 6 h and 12 h after 2-DG administration (1 h and 6 h, $n = 6$ mice for saline and 8 mice for 2-DG group; 12 h, $n = 12$ mice for saline and 15 mice for 2-DG group). **e**, Representative immunofluorescence of ATGL in the iBAT for 2-DG group. **e**, Representative immunofluorescence of ATGL in the iBAT collected 6 h after 2-DG administration. Scale bar, 20 μm . Representative images from three mice per group with similar results. **f**, Plasma FFA levels in the wild-type mice after 2-DG treatment for 5.5 h,

followed by insulin ($0.75 \text{ U kg}^{-1} \text{ BW}$) administration for 30 min ($n = 8$ mice per group). **g**, Plasma FFA levels in the wild-type mice 6 h after co-administration of 2-DG and insulin ($n = 8$ mice per group). **h,i**, Quantification of ATGL and HSL^{Ser660ph} levels in the subcutaneous adipose tissue taken before and after EHC from patients with insulin sensitivity or resistance ($n = 16$ patients with insulin sensitivity in **h**; $n = 8$ patients with insulin resistance in **i**). Data are presented as mean \pm s.e.m. and analysed using two-tailed unpaired *t*-test (**a–d** (1 h in liver, iBAT, 1 h and 6 h in iWAT, and 1 h and 6 h in gWAT)), two-tailed paired *t*-test (**i**), two-tailed Mann–Whitney test (**d** (6 h and 12 h in liver, 12 h in iWAT and 12 h in gWAT)), two-tailed Wilcoxon test (**h**) and one-way ANOVA method with Tukey correction (**f** and **g**). Source numerical data are available in .

repressing lipolysis to promote lipid storage^{1,6,7}. Conversely, hormonal or sympathetic-neuronal stimulation activates lipolysis to supply FAs^{1,8}.

HSL is activated by phosphorylation through catecholamine signalling activated protein kinase A (PKA)⁹. Insulin suppresses this process via phosphodiesterase 3B (PDE3B)-mediated cAMP degradation^{10,11}. Nevertheless, loss of HSL leads to mild phenotypes in both humans and mice^{1,5,12}. For example, liver-specific depletion of HSL does not impact hepatic TG levels and loss of HSL in adipose tissue leads to an age-dependent hepatic steatosis¹³. In contrast, *Atgl* loss of function in mice or humans leads to substantial LD accumulation^{14,15}. Liver-specific *Atgl* knockout mice exhibit hepatic LD accumulation, whereas adipose tissue-specific *Atgl* knockout mice display substantially reduced lipid

levels in the liver^{16,17}. ATGL function is modulated at multiple levels to meet complex physiological demands. Transcriptionally, insulin signalling inhibits *ATGL* messenger RNA synthesis⁶. At the post-translational level, catecholamine and glucagon signalling promote ATGL enzymatic activity through PKA- and CAMKII-mediated phosphorylation of ATGL at Ser406 in adipocytes and hepatocytes^{18,19}. In addition, ATGL abundance can be regulated by proteasome-mediated degradation after polyubiquitination via different E3 ligases, such as COPI and PEX2 (refs. 20,21).

The Golgi apparatus incorporates integral proteins spanning the membrane or recruits cytosolic proteins via interaction with Golgi-enriched lipids, such as PtdIns4P²². Owing to its negatively charged property, PtdIns4P can interact with proteins containing positively charged regions,

such as NLRP3 and STUB1, thereby enabling Golgi PtdIns4P to regulate inflammation and protein degradation, respectively^{23,24}. The Golgi PtdIns4P pool is mainly generated by the lipid kinases PI4KB²². Conversely, the lipid phosphatase SACMIL dephosphorylates PtdIns4P²². SACMIL activity is modulated via altered distribution in the ER and Golgi, and enrichment of SACMIL in the latter compartment is promoted by glucose or serum deprivation, leading to a reduction of PtdIns4P levels in the Golgi^{25,26}.

So far, hormone signalling is still the best-documented mechanism to coordinate glucose availability and systemic lipolysis. In this Article, we aimed to investigate cell-intrinsic mechanisms that balance the supply of glucose and FAs by regulation of lipolysis via intracellular glucose sensing. We identified a central role for PtdIns4P in the assembly of the E3 ligase complex CUL7^{FBXWS} in the Golgi, which in turn polyubiquitylates ATGL for proteasome-targeted degradation. Depletion of intracellular glucose is sensed by this pathway, leading to reduced assembly of the E3 ligase complex and increased ATGL-driven lipolysis.

Results

Glucose deprivation elevates ATGL-driven lipolysis

Previous work demonstrated that intracellular FAs modulate ATGL-driven lipolysis²⁰. To elucidate whether other cell-autonomous mechanisms modulate lipolysis in response to nutrient availability, we fasted mice for 24 h, which led to an increase in plasma free fatty acids (FFAs) (Fig. 1a). Next, we analysed the levels of lipolytic proteins, including ATGL, phosphorylated HSL, HSL, MGL, perilipin 1 (PLIN1) and comparative gene identification-58 (CGI-58), in the liver and adipose depots from fasted mice. Interestingly, only ATGL levels were significantly increased in the interscapular brown adipose tissue (iBAT), inguinal white adipose tissue (iWAT) and liver (Fig. 1b and Extended Data Fig. 1a), while both iWAT and gonadal white adipose tissue (gWAT) displayed upregulated pHSL levels (Extended Data Fig. 1a). To understand the time course of HSL phosphorylation and ATGL upregulation in response to long-term glucose deprivation, mice were treated with 2-deoxy-D-glucose (2-DG) to mimic glucose deprivation, *in vivo* (Extended Data Fig. 1b–e). Like fasting, glucose deprivation significantly induced lipolysis rapidly after 2-DG treatment (Fig. 1c), suggesting the molecular pathways involved may not rely on transcriptional regulation. To analyse the hormonal axis, we first determined levels of plasma insulin and observed reduction of insulin levels only 1 h after 2-DG administration (Extended Data Fig. 1f). Thus, we next quantified the main players involved in lipolysis in both liver and adipose depots at different timepoints. Intriguingly, upregulation of HSL phosphorylation was observed in WAT 1 h after 2-DG administration, while ATGL protein levels were increased in the liver and iBAT after 1 h and showed further accumulation in the liver, iBAT, iWAT and gWAT in response to longer glucose deprivation (Fig. 1d,e and Extended Data Fig. 1g,h), suggesting that ATGL regulation maintains higher lipolysis levels throughout glucose deprivation via a yet unknown mechanism. Hence, we tested the immediate effect of insulin on long-term glucose-deprived mice 6 h after 2-DG treatment. Unexpectedly, lipolysis levels were only partially suppressed and levels of pHSL and ATGL remained unchanged in the background of glucose deprivation 30 min after insulin treatment (Fig. 1f

and Extended Data Fig. 2a). Moreover, the anti-lipolytic effect of insulin was totally absent during long-term glucose deprivation (Fig. 1g). These observations led us to postulate the existence of cell intrinsic mechanisms of ATGL-driven lipolysis regulation via sensing intracellular glucose availability, independently of hormone signalling. To assess human relevance, we obtained subcutaneous fat from patients collected before and after euglycaemic hyperinsulinaemic clamp (EHC), corresponding to the low and high circulated glucose states, respectively. Higher ATGL levels were observed in subcutaneous adipose tissues before EHC in patients with either insulin sensitivity or insulin resistance (Fig. 1h,i), suggesting that a similar ATGL regulation occurs in humans.

We examined *Atgl* transcript levels in liver and adipose depots from fasted or glucose-deprived mice and found that *Atgl* transcript levels were unchanged, further indicating that the regulation is not dependent on transcriptional events (Extended Data Fig. 2b–d). In contrast, long-term fasting and glucose deprivation promoted *Atgl* transcript levels in the liver (Extended Data Fig. 2b–d), possibly due to hepatic PPAR α activation⁸. As adipose tissue is known to contribute to FA release⁸, we examined whether ATGL upregulation in the adipose tissue caused elevated plasma FFA levels during glucose deprivation. Therefore, we took advantage of liver- and adipose tissue-specific *Atgl* knockout mice (*Atgl* LKO and *Atgl* AKO mice) and found that only adipocytic ATGL was essential for increased plasma FFA levels in response to glucose deprivation (Extended Data Fig. 2e–h). Taken together, we demonstrate the existence of a cell-intrinsic mechanism of ATGL-driven lipolysis via sensing glucose availability, independently of insulin signalling.

Glucose deprivation stabilizes ATGL in the Golgi apparatus

As ATGL was predominantly regulated at the protein levels, we focused on the mechanism of ATGL stabilization in response to glucose availability. In agreement with the *in vivo* data, we observed that both glucose withdrawal and 2-DG treatment strongly induced ATGL protein abundance without changing transcript levels in HepG2 cells (Fig. 2a,b and Extended Data Fig. 3a,b). This finding was first corroborated in immortalized brown adipocytes (iBAs) (Fig. 2c–f and Extended Data Fig. 3c,d). In addition, we observed upregulation of ATGL protein in HEK293T and HEK293-AAV cells upon glucose deprivation (Fig. 2g,h and Extended Data Fig. 3e,f). Moreover, when we removed serum, amino acids as well as FAs from the culture medium we observed that only serum deprivation promoted the accumulation of ATGL protein (Extended Data Fig. 3g–i).

After being synthesized in the ER, ATGL is transported to the Golgi, where it translocates to the LD surface via elusive mechanisms²⁷. Inhibition of this process strongly reduces intracellular ATGL protein levels, highlighting the importance of the Golgi–LD axis in modulating ATGL abundance and function^{27,28}. Therefore, we focused on the LDs and Golgi as potential sites for the regulation of ATGL protein levels. First, we isolated LDs from HepG2 cells and observed that ATGL levels increased in the LDs fraction upon glucose deprivation (Extended Data Fig. 3j). Next, we treated HepG2 cells with inhibitors of DGAT1 and DGAT2, the key enzymes for the esterification of FAs, to deplete LDs (Extended Data Fig. 3k). Intriguingly, even in the absence of LDs, glucose deprivation

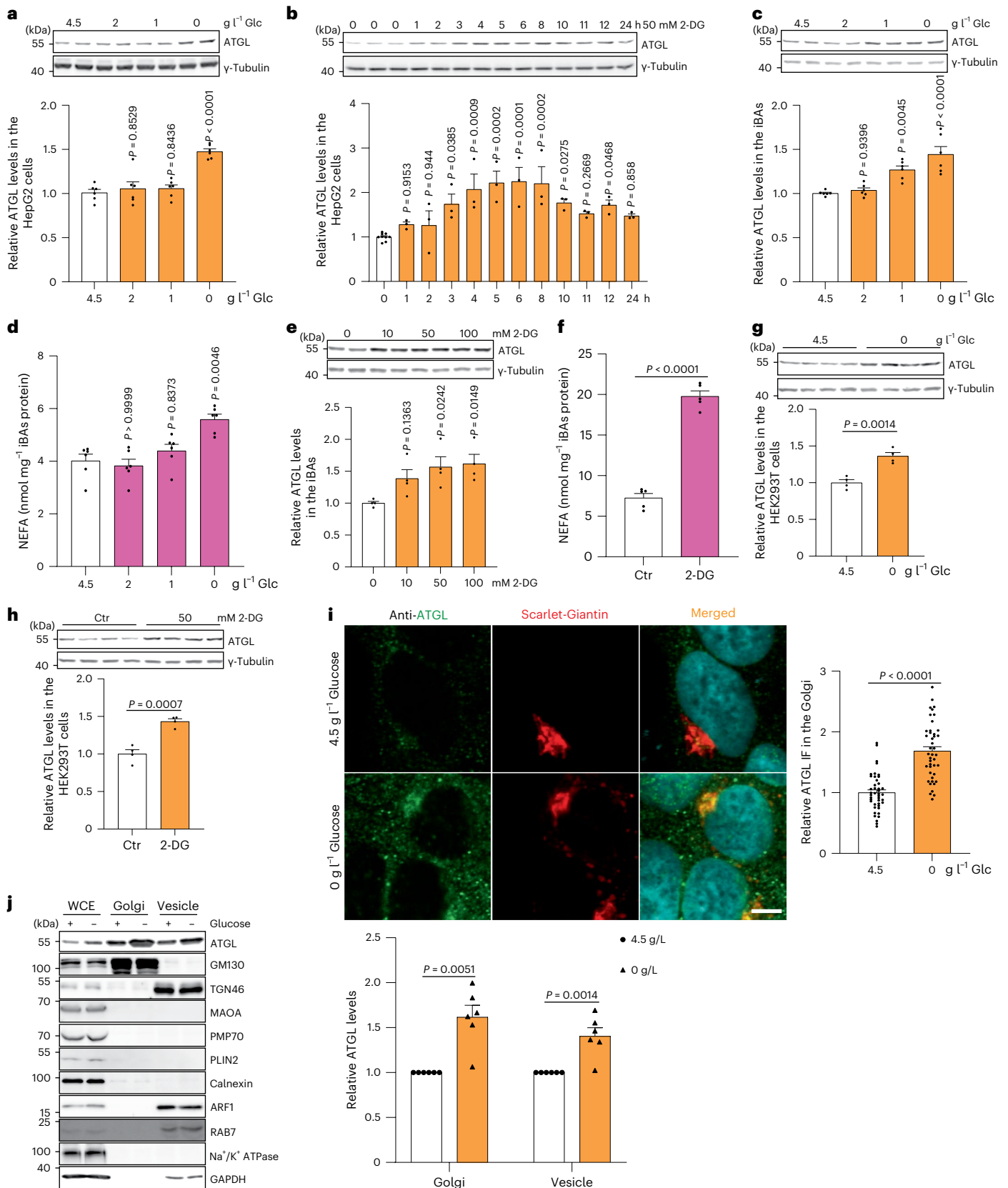
Fig. 2 | Glucose deprivation modulates lipolysis via stabilizing ATGL in the Golgi.

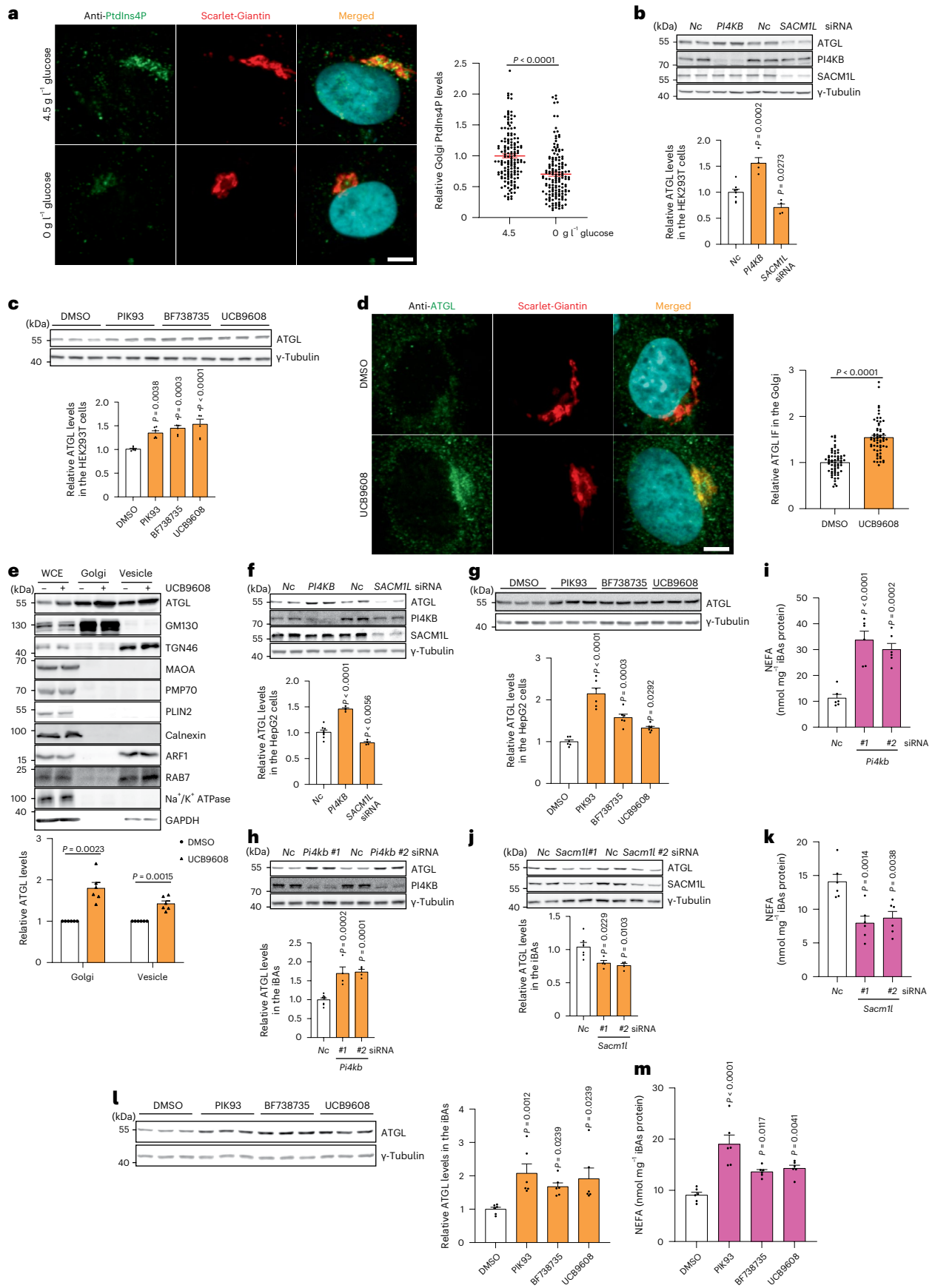
a, Immunoblot of ATGL in HepG2 cells cultured at different glucose (Glc) concentrations for 6 h ($n = 6$ independent experiments per group). **b**, Immunoblot of ATGL in HepG2 cells treated with 50 mM 2-DG and collected at indicated timepoints ($n = 9$ or 3 independent experiments for control or 2-DG groups). **c**, Immunoblot of ATGL in iBAs cultured at different glucose concentrations for 24 h ($n = 6$ independent experiments per group). **d**, Levels of NEFAs in the starvation medium released by iBAs in the basal state 24 h after treatment with medium at different glucose concentrations ($n = 6$ independent experiments per group). **e**, Immunoblot of ATGL in iBAs treated with 2-DG at indicated concentrations for 24 h ($n = 4$ independent experiments per group). **f**, Levels of NEFAs in the starvation medium released by iBAs in the basal state 24 h after treatment with control vehicle (Ctr) and 100 mM 2-DG ($n = 5$ independent

experiments per group). **g**, Immunoblot of ATGL in HEK293T cells 6 h after glucose withdrawal ($n = 4$ independent experiments per group). **h**, Immunoblot of ATGL in HEK293T cells 12 h after treatment with Ctr and 50 mM 2-DG ($n = 4$ independent experiments per group). **i**, Immunofluorescence of ATGL in HEK293-AAV cells 6 h after treatment with glucose free medium ($n = 43$ cells per group). Scale bar, 5 μ m. **j**, Immunoblot of ATGL in the WCE, Golgi and vesicle fractions extracted from HEK293T cells 6 h after glucose withdrawal ($n = 6$ independent experiments per group). Results are shown as mean \pm s.e.m. and analysed using two-tailed unpaired *t*-test (**f–i**), two-tailed paired *t*-test (**j**), one-way ANOVA method with Dunnett correction for multiple comparisons between control and other groups (**a–c** and **e**) and Kruskal–Wallis test with Dunn's correction for multiple comparisons between control and other groups (**d**). Source numerical data and unprocessed blots are available in .

could still increase endogenous ATGL levels (Extended Data Fig. 3l,m). Conversely, we did not observe any changes in intracellular ATGL levels upon glucose deprivation after treatment with Brefeldin A (BFA), a fungal toxin which blocks Golgi formation (Extended Data Fig. 3n–p). Therefore, we quantified ATGL levels in the Golgi by immunostaining

and fractionation and observed significantly elevated protein levels in the Golgi and vesicle fractions in response to glucose deprivation (Fig. 2i,j). These data demonstrate that ATGL is primarily regulated in the Golgi and subsequently translocated to its functional site on the LD surface for lipolysis modulation.





Reduction of Golgi PtdIns4P levels promotes ATGL stability
Both glucose and serum deprivation have been reported to reduce Golgi PtdIns4P levels in various cell types, which is mainly mediated by

promoting the retention of SACM1L in the Golgi after transfer from the endoplasmic reticulum (ER)^{25,26}. Therefore, we hypothesized that reduction of Golgi PtdIns4P levels during nutrient shortage might stabilize

Fig. 3 | Golgi PtdIns4P regulates ATGL protein stability in the Golgi apparatus. **a**, Immunofluorescence of PtdIns4P in HEK293-AAV cells after glucose deprivation ($n = 150$ cells per group). Scale bar, 5 μm . **b**, Immunoblot of ATGL in HEK293T cells 72 h after *PI4KB* and *SACMIL* knockdown ($n = 8$ or 4 independent experiments for control or other groups). **c**, Immunoblot of ATGL in HEK293T cells 24 h after treatment with 5 μM PIK93, 10 μM BF738735 and 10 μM UCB9608 ($n = 6$ independent experiments per group). **d**, Immunofluorescence of ATGL in HEK293-AAV cells 24 h after UCB9608 treatment ($n = 61$ cells per group). Scale bar, 5 μm . **e**, Immunoblot of ATGL in the different fractions from HEK293T cells 6 h after UCB9608 treatment ($n = 6$ independent experiments per group). **f**, Immunoblot of ATGL in HepG2 cells 72 h after *PI4KB* and *SACMIL* knockdown ($n = 8$ or 4 independent experiments for control or other groups). **g**, Immunoblot of ATGL in HepG2 cells 24 h after treatment with PIK93, BF738735 and UCB9608 ($n = 6$ independent experiments per group). **h, i**, Immunoblot of ATGL and

determination of basal lipolysis 72 h after knocking down *Pi4kb* in the iBAs ($n = 8$ or 4 independent experiments for control or other groups in **h**; $n = 6$ independent experiments per group in **i**). **j, k**, Immunoblot of ATGL and determination of basal lipolysis 72 h after knocking down *Sacm1l* in the iBAs ($n = 6$ or 4 independent experiments for control or other groups in **j**; $n = 6$ independent experiments per group in **k**). **l, m**, Immunoblot of ATGL (**l**) and determination of basal lipolysis (**m**) 24 h after treating iBAs with 1 μM PIK93, 1 μM BF738735 and 1 μM UCB9608 ($n = 6$ independent experiments per group). Data are presented as mean \pm s.e.m. and analysed using two-tailed paired *t*-test (**e**), two-tailed Mann–Whitney test (**a** and **d**), one-way ANOVA method with Dunnett correction for multiple comparisons between control and other groups (**b, c, f–k** and **m**) and Kruskal–Wallis test with Dunn's correction for multiple comparisons between control and other groups (**l**). Source numerical data and unprocessed blots are available in .

ATGL and, in turn, promote lipolysis. Firstly, we examined Golgi PtdIns4P levels via a P4M–EGFP sensor and a PtdIns4P antibody²⁹. We observed a reduction of Golgi PtdIns4P levels in conjunction with enrichment of SACMIL in the Golgi after glucose withdrawal (Fig. 3a and Extended Data Fig. 4a–c). The glucose deprivation reduced Golgi PtdIns4P levels independently of AMPK (Extended Data Fig. 4d,e). To study the effects of Golgi PtdIns4P on lipolysis, we genetically manipulated Golgi PtdIns4P levels via small interfering RNA (siRNA)-mediated knockdown of *PI4KB* and *SACMIL*²² (Extended Data Fig. 4f,g). Interestingly, we observed that Golgi PtdIns4P reduction led to elevated ATGL levels, whereas Golgi PtdIns4P accumulation decreased ATGL protein abundance (Fig. 3b and Extended Data Fig. 4h). Moreover, we used three PI4KB inhibitors to block Golgi PtdIns4P generation, and all three compounds elevated both endogenous and ectopically expressed ATGL protein levels (Fig. 3c and Extended Data Fig. 4i–k). As with glucose deprivation, ATGL protein accumulated in the Golgi when synthesis of Golgi PtdIns4P was blocked (Fig. 3d,e), indicating that Golgi PtdIns4P levels are crucial in determining the stability of ATGL. As glucose deprivation promoted ATGL-mediated lipolysis in different cell types, we examined the impact of Golgi PtdIns4P levels on this process in hepatocytes and adipocytes. We confirmed that the reduction of Golgi PtdIns4P increased both endogenous and ectopically expressed ATGL while upregulation had the opposite effect in hepatocytes (Fig. 3f,g and Extended Data Fig. 5a). Likewise, genetic depletion and pharmacological inhibition of PI4KB promoted ATGL stability and lipolysis whereas SACMIL depletion suppressed this process in adipocytes (Fig. 3h–m and Extended Data Fig. 5b,c).

Considering the relationship between glucose deprivation and Golgi PtdIns4P, as well as their roles in ATGL stabilization, we next studied whether glucose deprivation could regulate ATGL degradation via Golgi PtdIns4P. We first analysed ATGL regulation in response to glucose deprivation in the presence of SACMILK2A overexpression (Extended Data Fig. 5d), a Golgi resident mutant of SACMIL to reduce Golgi PtdIns4P levels²⁶. Furthermore, we depleted PtdIns4P in the Golgi by UCB9608-mediated inhibition of PI4KB. The loss of ATGL regulation after SACMILK2A overexpression and UCB9608 treatment suggests that reduction of Golgi PtdIns4P levels is not only required for

glucose deprivation induced ATGL upregulation, but also sufficient to increase ATGL levels even under high-glucose conditions (Extended Data Fig. 5e,f). Collectively, we could show that glucose availability regulates the distribution of SACMIL between ER and Golgi and modulates Golgi PtdIns4P levels, which in turn governs lipolysis by regulating ATGL stability in the Golgi.

CUL7^{FBXW8} regulates ATGL in the Golgi apparatus

Although ATGL is regulated in the Golgi, it remains unclear how Golgi PtdIns4P levels could modulate ATGL stability. Given that proteasome-mediated degradation and autophagy are the main pathways to degrade intracellular proteins, we blocked both processes by MG132 and chloroquine treatment, respectively³⁰. Interestingly, only MG132 treatment led to the cellular accumulation of ATGL protein (Extended Data Fig. 6a), indicating that ATGL degradation is executed by the proteasome. K48-linked polyubiquitylation of substrates acts as the main signal for proteasome-mediated degradation³⁰. We thus examined whether lysine ubiquitylation of ATGL is dispensable for its regulation upon glucose deprivation. Therefore, we constructed a lysine null ATGL mutant²⁰, and analysed its accumulation after glucose-free medium and 2-DG treatments (Extended Data Fig. 6b,c). In contrast to wild-type ATGL, the lysine null ATGL mutant was unresponsive to either treatment (Extended Data Fig. 6b,c). Furthermore, K48-linked polyubiquitylation of ATGL was reduced upon glucose deprivation (Extended Data Fig. 6d,e). These observations suggest the presence of a Golgi resident E3 ligase to sense glucose availability and polyubiquitylate ATGL for proteasome-mediated degradation.

To identify the E3 ligase responsible for glucose deprivation-induced ATGL accumulation in the Golgi, we performed a small screen of E3 ligases, which are reportedly localized to the Golgi, and the well-known Golgi PtdIns4P effectors mediating the functions of PtdIns4P in Golgi organization, membrane trafficking and protein secretion (Extended Data Fig. 6f–i)^{31–35}. Among them, we observed that only depletion of CUL7 and FBXW8, was able to significantly elevate ATGL levels in both the whole-cell extract (WCE) and the Golgi fraction (Fig. 4a–c and Extended Data Fig. 6j–l). Furthermore, depletion of either component substantially

Fig. 4 | The Golgi resident E3 ligase complex CUL7^{FBXW8} polyubiquitylates ATGL for degradation. **a**, Quantification of ATGL protein levels in HEK293T WCE in a small-scale siRNA screen via immunoblot ($n = 18$ or 3 independent experiments for control or other groups). **b**, Immunofluorescence of ATGL in HEK293-AAV cells 72 h after *CUL7* & *FBXW8* knockdown ($n = 61$ cells per group). Scale bar, 5 μm . **c**, Immunoblot of ATGL in the WCE, Golgi and vesicle fractions extracted from HEK293T cells 72 h after *CUL7* & *FBXW8* knockdown ($n = 6$ independent experiments per group). Asterisk indicates a non-specific band. **d**, Immunoblot of ATGL in HepG2 cells 72 h after *CUL7* and *FBXW8* knockdown ($n = 8$ or 4 independent experiments for control or other groups). **e**, Representative images of LDs stained by BODIPY in HepG2 cells 72 h after siRNA knockdown. Scale bar, 20 μm . Three times repeated independently with similar results. **f**, Immunoblot of ATGL in iBAs 72 h after *Cul7* and *Fbxw8* knockdown ($n = 8$ or 4 independent experiments for control or other groups). **g**, Levels of

NEFAs in the starvation medium released by iBAs in the basal state 72 h after knockdown of *Cul7* and *Fbxw8* ($n = 6$ independent experiments per group). **h**, Co-IP conducted in HEK293T WCE by FLAG antibody 48 h after expressing ATGL–FLAG or FBXW8–FLAG. Three times repeated independently with similar results. **i**, K48-linkage polyubiquitylation pattern detection in HEK293T cells transfected with ATGL–FLAG, followed by siRNA transfection for 72 h and IP to enrich ATGL–FLAG. Four times repeated independently with similar results. **j**, Immunoblot of ATGL in HEK293T cells 6 h after glucose withdrawal in the absence of CUL7^{FBXW8} ($n = 5$ independent experiments per group). Data are presented as mean \pm s.e.m. and analysed using two-tailed unpaired *t*-test (**b** and **j**), two-tailed paired *t*-test (**c**), one-way ANOVA method with Dunnett correction for multiple comparisons between control and other groups (**a, d** and **f**) and Kruskal–Wallis test with Dunn's correction for multiple comparisons between control and other groups (**g**). Source numerical data and unprocessed blots are available in .

reduced LD levels, dependent on the presence of ATGL (Extended Data Fig. 6m). The scaffold protein CUL7 interacts with substrate receptor FBXW8 to form a functional E3 ligase complex^{36,37}. Moreover, the presence of a positively charged polybasic region, a putative interactor of negatively charged PtdIns4P^{23,24}, in the N-terminus of FBXW8 might allow the CUL7^{FBXW8} E3 ligase complex to sense glucose availability. Before testing this hypothesis, we first analysed the function of CUL7^{FBXW8} in hepatocytes and adipocytes. Depletion of CUL7^{FBXW8} resulted in higher ATGL protein levels, as well as an ATGL-dependent decline of LD abundance and lipolysis upregulation (Fig. 4d–g and Extended Data Fig. 6n,o). Therefore, we measured the physical interaction between FBXW8 and ATGL by co-immunoprecipitation (co-IP). We observed a direct interaction of FBXW8 and ATGL (Fig. 4h), as well as reduced K48-linked polyubiquitylation levels of ATGL, after CUL7^{FBXW8} depletion, which demonstrates that CUL7^{FBXW8} interacts with ATGL in the Golgi for polyubiquitylation and proteasome-mediated degradation (Fig. 4i). Lastly, we examined ATGL regulation upon glucose deprivation in the absence of CUL7^{FBXW8} and found that glucose sensing was abolished under this condition (Fig. 4j). Taken together, these data show that the Golgi resident E3 ligase complex CUL7^{FBXW8} is essential to regulate polyubiquitylation and degradation of ATGL in response to glucose deprivation.

Golgi PtdIns4P Regulates CUL7^{FBXW8} function

CUL7 and FBXW8 were previously shown to localize to the Golgi of certain cell types^{32,38}. To understand how CUL7^{FBXW8} senses glucose availability and, in turn, regulates ATGL degradation, we next examined the cellular localization of CUL7 and FBXW8 by immunostaining. In line with previous reports and our fractionation result, endogenous CUL7 was highly enriched in the Golgi, instead of vesicles (Figs. 4c and 5a). Unexpectedly, however, both endogenously and ectopically expressed FBXW8 exhibit a dispersed pattern, with a certain portion of localization in the Golgi (Figs. 4c and 5a). In contrast, it was barely detectable in the vesicle fraction (Fig. 4c). Considering the existence of the polybasic region in the N terminus of FBXW8, we hypothesized that Golgi PtdIns4P might be able to recruit FBXW8 to the Golgi where it would be assembled into a functional E3 ligase complex. Therefore, we examined CUL7 and FBXW8 levels in the Golgi upon glucose deprivation via fractionation and immunostaining. As expected, FBXW8 instead of CUL7 displayed reduced levels in the Golgi (Fig. 5b and Extended Data Fig. 7a,b). Next, we depleted Golgi PtdIns4P, which led to reduced FBXW8 distribution to the Golgi (Fig. 5c and Extended Data Fig. 7c), indicating that FBXW8 distribution is dependent on Golgi PtdIns4P. To demonstrate the interaction between the polybasic region of FBXW8 and PtdIns4P, we built a FLAG-tagged wild-type FBXW8 and an FBXW8 mutant in which all lysine and arginine residues in the polybasic region of FBXW8 were mutated to alanine (Fig. 5d and Extended Data Fig. 7d). We purified recombinant FBXW8 proteins and examined their binding capacity with various lipid species using a membrane lipid strip. Among the tested lipid species, PtdIns4P displayed a binding capacity to wild-type FBXW8 whereas the interaction was lower between PtdIns4P and the mutant FBXW8 (Extended Data Fig. 7e). These data were further confirmed using PIP strips and PtdIns4P-conjugated agarose beads (Fig. 5e,f).

After demonstrating the physical interaction between the polybasic region of FBXW8 and PtdIns4P, we next examined whether the

recruitment of FBXW8 to the Golgi was affected by glucose availability. In agreement with its PtdIns4P interaction capacity, wild-type FBXW8 levels in the Golgi were reduced upon glucose deprivation, while mutant FBXW8 was not sensitive to glucose levels (Fig. 5g,h). In conclusion, glucose deprivation leads to lower levels of Golgi PtdIns4P, which interacts with the polybasic region of FBXW8 for its recruitment to the Golgi, where the CUL7^{FBXW8} E3 ligase complex is assembled to polyubiquitylate ATGL for proteasomal degradation (Fig. 5i).

Golgi PtdIns4P regulates ATGL-driven lipolysis in mice

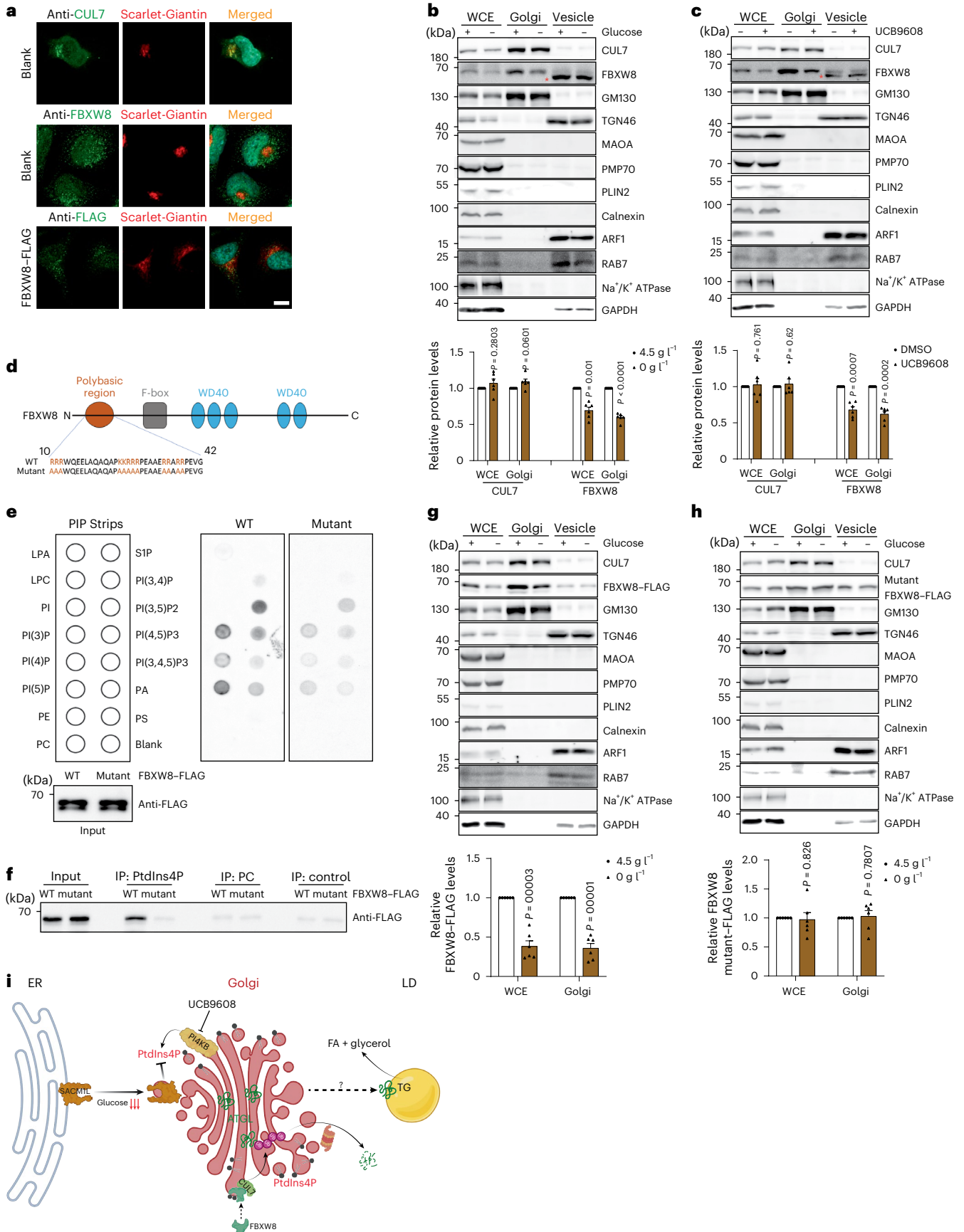
Our data identify Golgi PtdIns4P as the central player regulating ATGL-driven lipolysis, thus coupling glucose availability and intracellular FA liberation. Therefore, we focused on liver ATGL regulation as a key factor in hepatic lipolysis and TG accumulation, especially under conditions of MASLD pathogenesis^{16,39}. To manipulate Golgi PtdIns4P levels in the liver, we administered *LSL-spCAS9* mice with guide RNAs (gRNAs) expressing AAV8 viruses to knock out *Pi4kb*, *Sacm1l*, *Cul7* or *Fbxw8* specifically in hepatocytes. This approach led to an efficient depletion of PI4KB protein levels in the liver 2 weeks after AAV8 administration (Fig. 6a). In the absence of PI4KB, ATGL protein levels were significantly upregulated (Fig. 6a and Extended Data Fig. 8a). Global depletion of *Sacm1l* has been reported to cause embryonic lethality⁴⁰, and we found that liver-specific depletion of *SACM1L* was also lethal, which impedes any mechanistic investigation. Depletion of CUL7 led to a destabilization of FBXW8 in the liver but not vice versa (Fig. 6b). This is in contrast to previous reports demonstrating that these two factors can stabilize each other^{36,37}. We observed increased ATGL levels after knockout of *Cul7* and *Fbxw8* in the liver (Fig. 6b and Extended Data Fig. 8b), indicating a consistent *in vivo* role for CUL7^{FBXW8}. Next, we examined whether the E3 ligase complex CUL7^{FBXW8} is responsible for hepatic ATGL upregulation in response to glucose deprivation. Therefore, we administered 2-DG to *Cul7* and *Fbxw8* double knockout mice, which led to upregulation of hepatic ATGL levels of wild-type mice but not in the absence of CUL7^{FBXW8} (Fig. 6c), underscoring the essential role of CUL7^{FBXW8} in regulating glucose-deprivation-induced ATGL stabilization.

Upregulation of hepatic ATGL levels is reported to counteract TG deposition in the fatty liver³⁹. Therefore, we examined the physiological and pathophysiological effects in MASLD model after genetic and pharmacological manipulation of the Golgi PtdIns4P–CUL7^{FBXW8}–ATGL axis. Indeed, PI4KB depletion decreased hepatic TG levels (Fig. 6d,e and Extended Data Fig. 8c,d). Moreover, when PI4KB was ablated in the MASLD mouse model induced with 12-week high-fat diet (HFD), TG deposition in the fatty liver was significantly reduced 8 weeks after virus administration (Fig. 6d,e and Extended Data Fig. 8c,d). Similarly, we determined hepatic TG levels in the *Cul7* and *Fbxw8* knockout mice under normal chow diet (NCD) feeding conditions and found that only CUL7 ablation reduced hepatic TG levels (Fig. 6f,g and Extended Data Fig. 8e,f). In contrast, depletion of either factor was able to reduce hepatic TG accumulation in mice challenged with HFD for 12 weeks (Fig. 6f,g and Extended Data Fig. 8e,f). In addition to genetic manipulation, we examined the effect of the PI4KB inhibitor on lipolysis regulation and MASLD progression. Therefore, wild-type mice were fed on HFD for 12 weeks to induce hepatic steatosis, and subsequently treated with UCB9608 (ref. 41) (Fig. 6h). PI4KB inhibition significantly increased

Fig. 5 | Recruitment of FBXW8 to the Golgi via interaction with PtdIns4P.

a, Representative photomicrographs of the immunofluorescence of CUL7, FBXW8 and ectopically expressed FBXW8–FLAG in HEK293-AAV cells stained by the indicated antibodies. Scale bar, 5 μ m. Repeated independently three times with similar results. **b,c**, Immunoblot of CUL7 and FBXW8 in the WCE, Golgi and vesicle fractions extracted from HEK293T cells after glucose withdrawal or UCB9608 treatment ($n = 6$ independent experiments per group). Asterisk indicates a non-specific band. **d**, Schematic illustration of the domains of human FBXW8. **e**, Blotting analysis of PIP strips incubated with recombinant proteins FBXW8–FLAG and FBXW8 mutant–FLAG. Three times repeated independently

with similar results. **f**, Immunoblot of recombinant protein FBXW8–FLAG and FBXW8 mutant–FLAG after pull-down by PtdIns4P agarose beads. Three times repeated independently with similar results. **g,h**, Immunoblot of FBXW8–FLAG and FBXW8 mutant–FLAG in the WCE, Golgi and vesicle fractions extracted from HEK293T cells after glucose withdrawal ($n = 6$ independent experiments per group). **i**, Schematic diagram illustrating the working model of the mechanism by which glucose availability is coupled to lipolysis via Golgi PtdIns4P. Results are shown as mean \pm s.e.m. and analysed using two-tailed paired *t*-test (**b, c, g** and **h**). Source numerical data and unprocessed blots are available in .



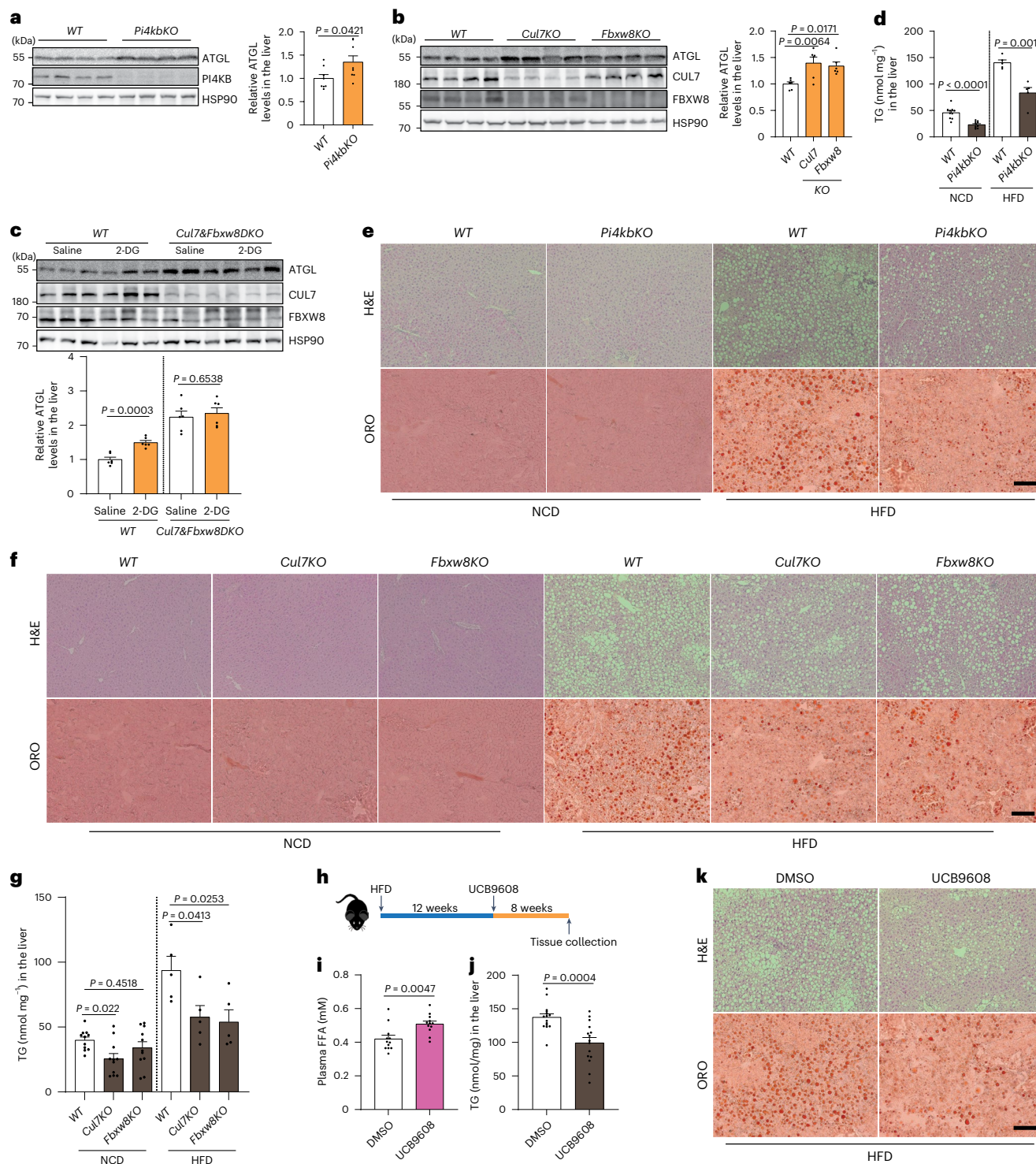


Fig. 6 | Regulation of lipolysis and MASLD development via manipulating Golgi PtdIns4P–CUL7^{FBXW8}–ATGL axis. **a**, Immunoblot of ATGL protein in the liver from hepatocyte-specific *Pi4kb* knockout mice 2 weeks after AAV8 administration ($n = 8$ mice per group). **b**, Immunoblot of ATGL protein in the liver from hepatocyte-specific *Cul7* and *Fbxw8* knockout mice 2 weeks after AAV8 administration ($n = 6$ mice per group). **c**, Immunoblot of ATGL protein in the liver 1 h after 2-DG injection under the background of *Cul7* and *Fbxw8* double knockout in the hepatocytes ($n = 6$ mice per group). **d**, Determination of hepatic TG levels in NCD feeding mice 4 weeks after AAV8 administration or HFD feeding mice 8 weeks after AAV8 administration ($n = 10$ mice per NCD group and 5 mice per HFD group). **e, f**, H&E and ORO staining to the liver from hepatocyte-specific *Pi4kb* (**e**), *Cul7* and *Fbxw8* (**f**) knockout mice under NCD and HFD feeding conditions. Scale bar, 200 μ m. Representative images from five mice per group

with similar results. **g**, Determination of hepatic TG levels in hepatocyte-specific *Cul7* and *Fbxw8* knockout mice fed in NCD and HFD after AAV8 administration ($n = 11$ mice per NCD group and 5 mice per HFD group). **h**, Schematic illustration of experimental design to administer UCB9608 to wild-type mice. **i**, Plasma FFA levels in wild-type mice 8 weeks after administration of DMSO and UCB9608 ($n = 12$ mice per group). **j**, Hepatic TG levels in DMSO- and UCB9608-treated mice ($n = 15$ mice per group). **k**, H&E and ORO stainings to the liver from DMSO- and UCB9608-treated mice. Scale bar, 200 μ m. Representative images from ten mice per group with similar results. Data are presented as mean \pm s.e.m. and analysed using two-tailed unpaired *t*-test (**a**, **c**, **d** and **j**), two-tailed Mann–Whitney test (**i**) and one-way ANOVA method with Dunnett correction for multiple comparisons between control and other groups (**b** and **g**). Source numerical data and unprocessed blots are available in .

plasma FFA levels (Fig. 6i and Extended Data Fig. 8g), suggesting a consistent *in vivo* role of Golgi PtdIns4P in regulating ATGL-driven lipolysis in the adipose tissue. Therefore, we compared the ATGL protein levels in different adipose depots and livers from dimethyl sulfoxide (DMSO)- and UCB9608-treated mice, and we found the latter displayed significantly greater ATGL protein levels in the iBAT, gWAT and liver with a similar trend in the iWAT (Extended Data Fig. 8h–l). In agreement with the reported role of ATGL upregulation in the adipose tissue⁴², UCB9608 treatment led to higher energy expenditure, possibly due to elevated FA levels that are used as a substrate for β -oxidation (Extended Data Fig. 8m–p). The enhancement of ATGL-driven lipolysis in the adipose tissue might contribute to increased FA liberation and release, whereas elevation of hepatic ATGL levels could drive intrahepatic lipolysis and reduce hepatic TG levels^{8,39}. Therefore, we determined hepatic TG levels in the livers of UCB9608-treated mice and observed substantially attenuated hepatic steatosis, dependent on the presence of liver ATGL (Fig. 6j,k and Extended Data Fig. 8q). In conclusion, we demonstrate that the Golgi PtdIns4P–CUL7^{FBXWS}–ATGL axis regulates hepatic ATGL levels and LD clearance, which could provide a potential target to ameliorate hepatic steatosis.

Reduction of Golgi PtdIns4P attenuates MASH progression

As we have demonstrated the potential applicability of the identified pathway for MASLD treatment, we further investigated whether targeting Golgi PtdIns4P production could attenuate MASH progression. To model MASH in the mouse liver⁴³, wild-type mice were housed under thermoneutral conditions on HFD diet plus high glucose- and fructose-containing drinking water for 24 weeks and were afterwards treated with UCB9608 for another 12 weeks (Fig. 7a). Interestingly, we observed that UCB9608 treatment induced a significant loss of body weight (BW) and fat mass, in agreement with the enhanced lipolysis and energy expenditure induced by UCB9608 (Fig. 7b–d and Extended Data Fig. 8m). Hence, we further examined TG levels as well as markers of hepatic toxicity. The reduction of all parameters upon UCB9608 treatment indicated amelioration of hepatic steatosis and injury, leading us to perform pathohistological analyses (Fig. 7e,f). We observed that UCB9608 treatment reduced liver mass/BW ratio and hepatic TG levels, in conjunction with elevated FA oxidation (Fig. 7g,h and Extended Data Fig. 9a). Consistently, steatosis grade, liver injury, inflammation levels, fibrosis grade and MASLD activity score were significantly lower in the livers from UCB9608-treated mice, suggesting suppressed MASH progression, although it should be noted that the MASH induction in these murine livers was relatively mild compared to clinical MASH in human patients (Fig. 7i,j and Extended Data Fig. 9b,c). The mitigation of inflammation and fibrosis markers upon UCB9608 treatment was further corroborated by quantifying transcript levels (Fig. 7k,l).

The progression of MASH may lead to cirrhosis and possibly hepatocellular carcinoma, and both pathological situations require liver transplantation to circumvent liver failure. Liver grafts cannot be transplanted when they are steatotic, thus requiring potential strategies to defatten

steatotic livers for clinical use. Given the ability of UCB9608 to ameliorate hepatic TG levels in mice, we tested the defatting effect of UCB9608 on a steatotic human liver during an *ex vivo* perfusion⁴⁴. We utilized a human liver graft with 15% macrovesicular steatosis and perfused the liver with blood for 8 days. UCB9608 was administered daily to reach a target concentration of 10 μ M (Fig. 7m). The graft displayed normal bile acid excretion and oxygen consumption, suggesting healthy status of the graft during the perfusion (Extended Data Fig. 9d,e). Interestingly, we detected non-esterified fatty acids (NEFAs) from dialysate during perfusion, suggesting an induction of lipolysis that resulted in the release of FAs (Extended Data Fig. 9f). To study the time course of liver defatting, we sampled biopsies from both lobes to determine ATGL and TG levels (Extended Data Fig. 9g). Consistent with the findings in mice, we observed substantially elevated ATGL levels after UCB9608 treatment in conjunction with reduced TG deposition while ATGL and hepatic TG levels remained unchanged in two control grafts, indicating a defatting effect mediated by ATGL-driven lipolysis upon UCB9608 administration (Fig. 7n,o and Extended Data Fig. 9h–j). Taken together, the discovery of Golgi PtdIns4P-mediated ATGL stabilization in response to glucose deprivation might be a promising therapeutic strategy to counteract MASH progression and might also serve as a potential therapeutic approach to repair steatotic liver grafts, *ex vivo*.

Discussion

It is well known that the endocrine system plays important roles in glucose and FA handling during different nutritional states. Insulin promotes *de novo* lipogenesis to produce FAs using excess glucose as a carbon source, and at the same time it suppresses lipolysis to reduce FA release from lipid stores^{6,7}. Conversely, glucagon or norepinephrine are secreted in response to starvation or cold exposure, to boost lipolysis through ATGL and HSL phosphorylation in hepatocytes and adipocytes^{1,18}. Typically, such extracellular hormones rapidly initiate a systemic response to acute physiological alterations. However, hormone signalling usually does not act chronically due to corresponding receptor desensitization. This process is exemplified by classical β -arrestin-mediated desensitization of β 1 adrenergic receptors upon ligand binding^{45,46}, which might explain our results that elevated pHSL levels were reversed in the adipose tissue upon long-term glucose deprivation. This homeostatic feedback loop probably necessitated cells to develop intrinsic mechanisms to tune lipolysis to nutrient supplies as a complementary process to extracellular hormone-mediated regulation of lipid metabolism for the organism to meet complex physiological demands. The mechanism described here might reshape our understanding regarding the exact contribution of insulin signalling to lipolysis regulation as insulin could also modulate intracellular glucose levels to signal via the Golgi PtdIns4P–CUL7^{FBXWS}–ATGL axis for lipolysis regulation. Reduction of HSL phosphorylation is believed to be the main mediator of the anti-lipolytic role of insulin^{10,11}. Here we found that insulin does not suppress pHSL under conditions of glucose deprivation, suggesting that glucose itself is an important mediator of lipolytic function and possibly mediates the anti-lipolytic

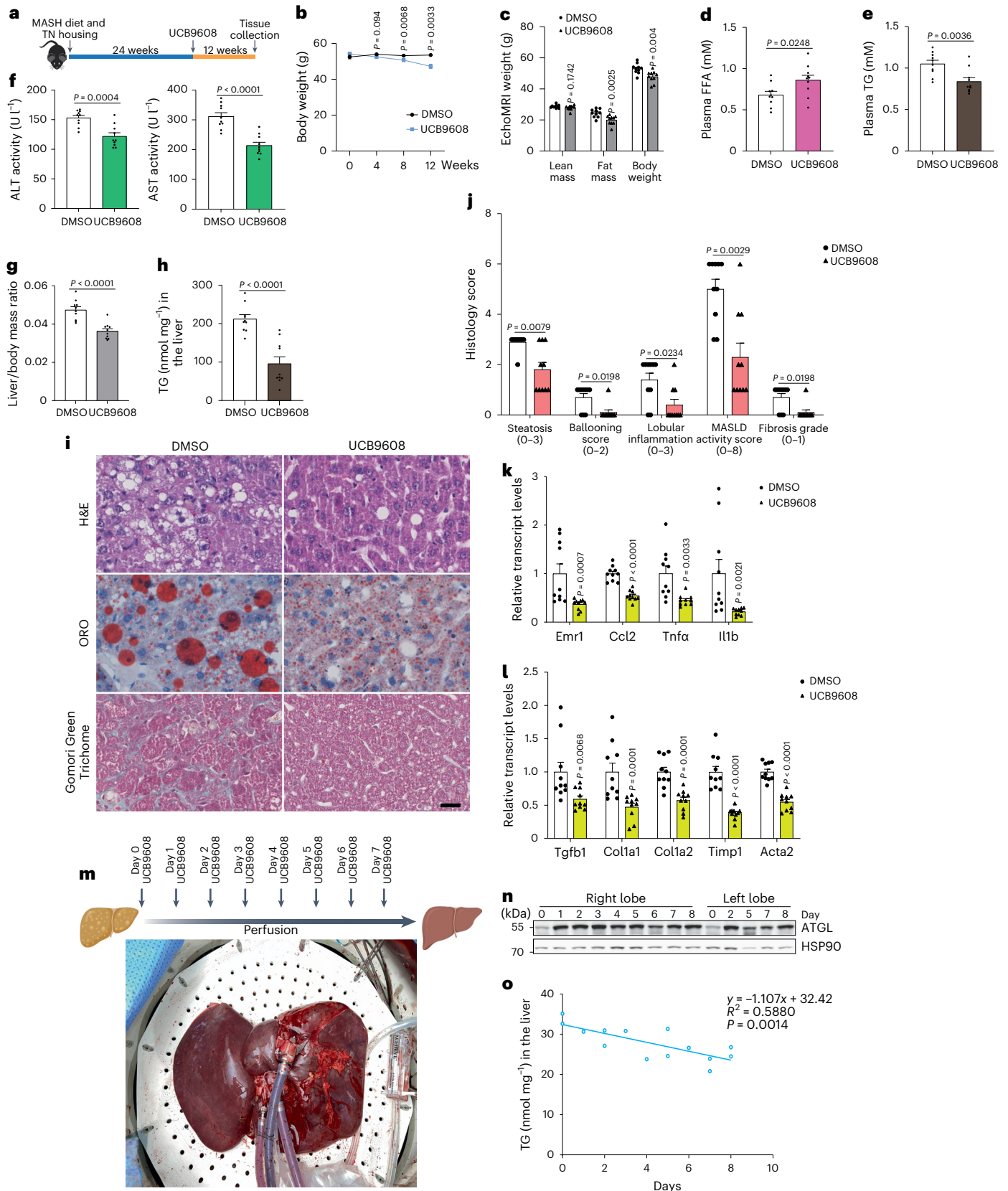
Fig. 7 | Amelioration of murine MASH progression and steatosis in human liver graft via blocking Golgi PtdIns4P generation. **a**, Schematic illustration of experiment design to administer UCB9608 to wild-type mice after induction of MASH via HFD, high-glucose/fructose-containing water and thermoneutral housing. **b**, BW gain during the period of UCB9608 treatment ($n = 10$ mice per group). **c**, EchoMRI analyses of lean mass, fat mass and BW to the MASH mice ($n = 10$ mice per group). **d,e**, Plasma FFA levels (**d**) and TG levels (**e**) 12 weeks after administration of UCB9608 ($n = 10$ mice per group). **f**, Alanine transaminase (ALT) and aspartate aminotransferase (AST) activity in the plasma from MASH mice after administration of UCB9608 ($n = 10$ mice per group). **g**, Liver mass/BW ratio of MASH mice after administration of UCB9608 ($n = 10$ mice per group). **h**, Determination of hepatic TG levels of MASH mice after administration of UCB9608 ($n = 10$ mice per group). **i**, Representative images of H&E staining, ORO staining and Gomori Green Trichrome staining. Scale bar, 25 μ m. Representative

images from ten mice per group with similar results. **j**, Histology score of livers from MASH mice treated by DMSO and UCB9608 ($n = 10$ mice per group). **k,l**, Transcript levels of inflammatory markers (**k**) and fibrosis markers (**l**) in MASH livers as determined by qPCR ($n = 10$ mice per group). **m**, Schematic illustration of experiment design to administer UCB9608 to a human liver graft *ex vivo* during normothermic machine perfusion. **n,o**, Immunoblot of ATGL protein and quantification of TG levels in the human liver biopsies taken at different timepoints from both lobes. Three times repeated technically with similar results. Results are shown as mean \pm s.e.m. and analysed using two-tailed unpaired *t*-test (**b–g** and **k** (Ccl2 and Tnf α) and **l** (Col1a2, Timp1 and Acta2)), two-tailed Mann–Whitney test (**h,j** and **k** (Emr1 and Il1b) and **l** (Tgfb1 and Col1a1)) and two-tailed Pearson's correlation (**o**). Source numerical data and unprocessed blots are available in .

effect of insulin. This might be especially relevant in insulin resistance as we found that patients with type 2 diabetes display increased ATGL levels upon fasting. It should be noted that the lack of precise glucose uptake data during EHC makes it difficult to detangle the effects mediated either by insulin or glucose availability. Notably, insulin receptor

substrate 1 (IRS1), a critical mediator of insulin signalling, is reported to be a substrate of CUL7^{FBXW8}, supporting a crosstalk between insulin and Golgi PtdIns4P-mediated regulation of lipolysis⁴⁷.

Although the electrostatic interaction between FBXW8 and negatively charged phospholipids is not specific to PtdIns4P as demonstrated



by our in vitro assays, the recruitment of FBXW8 to the Golgi could be facilitated by enriched PtdIns4P levels in the Golgi as subcellular compartments have unique phospholipid distribution patterns²². Previous reports have shown that CUL7^{FBXW8} assembly promotes the stability of CUL7 and FBXW8 as loss of either factor strongly reduces the protein levels of the other^{36,37}, and we found CUL7 depletion leads to destabilization of FBXW8. Consequently, FBXW8 levels in both Golgi and WCE are reduced since free FBXW8 is less stable in the cytosol. In contrast, we found that depletion of FBXW8 could only destabilize CUL7 in iBAs, suggesting that CUL7 is the major factor in stabilizing the E3 ligase complex. In line with this is our finding that CUL7 depletion has a stronger effect on ATGL upregulation. Although numerous E3 ligases have been reported to exist in the Golgi³², the sensitivity of the Golgi PtdIns4P–CUL7^{FBXW8}–ATGL axis to glucose availability identifies the CUL7^{FBXW8} complex as the key E3 ligase that mediates glucose deprivation-induced metabolic rewiring through polyubiquitylation of other substrates in addition to IRS1 and ATGL, which will require further studies.

In contrast to adipocytes, most non-adipocytes possess fewer LDs, and thus upon glucose or serum deprivation they have to initiate autophagic degradation of non-essential cellular components to provide carbon sources to generate LDs in proximity to mitochondria⁴⁸. The regulation of ATGL probably primes lipolysis activation in the starved cells for ATGL translocation from the Golgi to the LDs once the latter are generated. Although starvation elevates ATGL in the Golgi, vesicles and LDs, the regulation mainly takes place in the early Golgi, instead of the vesicles and LDs (Fig. 4C and Extended Data Fig. 3j). Moreover, whether and how Golgi derived vesicles and other types of intracellular vesicle mediate ATGL regulation as well as its translocation from Golgi to the LDs surface requires further investigations (Fig. 5i). In addition, abundant LDs can be artificially induced by oleic acid (OA)-containing medium in non-adipocytes. Under this condition, glucose or serum starvation can induce autophagic degradation of the LD coat proteins perilipin 2 and 3 (PLIN2/PLIN3), the clearance of which can empty the LD surface for ATGL localization and action⁴⁹. We observed that PLIN1 was not altered in adipose depots after fasting, suggesting that the regulation of lipolysis in adipocytes and non-adipocytes are distinctive features despite the existence of a common regulatory pathway.

Hepatosteatosis is mainly due to elevated FAs delivered from the circulation, in addition to elevated hepatic de novo lipogenesis, decreased hepatic lipolysis and FA oxidation in the hepatocytes^{50,51}. Inflammation is induced by secretion of inflammatory factors from the Kupffer cells while hepatic stellate cells are responsible for secretion of collagen that contributes to fibrosis⁵⁰. Based on our findings and other reported studies, Golgi PtdIns4P might serve as a potent target to block MASH progression as Golgi PtdIns4P also plays pivotal roles in NLRP3 activation via direct recruitment to the Golgi and thus the inflammation in the MASH liver probably can be directly alleviated by lowering the PtdIns4P levels^{23,52}. Further, procollagen, after being synthesized in the ER, traffics to the Golgi for secretion into the extracellular space. The formation of these vesicles might require the contribution of Golgi PtdIns4P to induce membrane curvature^{22,53}. If so, targeting PI4KB might be a very promising strategy to directly attenuate steatosis, inflammation and fibrosis in MASH. More importantly, UCB9608 treatment reduced plasma TG levels in the mouse MASH model, unlike elevated TG secretion and hypertriglyceridaemia observed upon administration of an acetyl-CoA carboxylase inhibitor in mice and humans⁵⁴. Considering that many PI4KB inhibitors have been developed to treat infectious diseases and cancer, such drugs could be repurposed to also treat MASH²². Interestingly, besides the defatting effect, UCB9608 is also known to exhibit immunosuppressive properties⁴¹. Considering immunosuppressive agents are necessary to prevent allograft rejection after organ transplantation, it will be a promising option to continue UCB9608 administration after engraftment if it is approved for clinical application.

In summary, our findings identify an intrinsic pathway that links glucose availability to lipid availability via glucose sensing by a Golgi

PtdIns4P–ATGL–lipolysis pathway that leads to the upregulation of lipolysis and the increased release of FAs from LD stores upon glucose depletion. By such means, cells can fine-tune nutrient flux in addition to paracrine hormone-mediated regulation of nutrient availability.

Online content

Any methods, additional references, Nature Portfolio reporting summaries, source data, extended data, supplementary information, acknowledgements, peer review information; details of author contributions and competing interests; and statements of data and code availability are available at <https://doi.org/10.1038/s41556-024-01386-y>.

References

- Zechner, R., Madeo, F. & Kratyk, D. Cytosolic lipolysis and lipophagy: two sides of the same coin. *Nat. Rev. Mol. Cell Biol.* **18**, 671–684 (2017).
- Singh, R. et al. Autophagy regulates lipid metabolism. *Nature* **458**, 1131–1135 (2009).
- Schott, M. B. et al. Lipid droplet size directs lipolysis and lipophagy catabolism in hepatocytes. *J. Cell Biol.* **218**, 3320–3335 (2019).
- Zimmermann, R. et al. Fat mobilization in adipose tissue is promoted by adipose triglyceride lipase. *Science* **306**, 1383–1386 (2004).
- Osuga, J. et al. Targeted disruption of hormone-sensitive lipase results in male sterility and adipocyte hypertrophy, but not in obesity. *Proc. Natl Acad. Sci. USA* **97**, 787–792 (2000).
- Chakrabarti, P. & Kandror, K. V. FoxO1 controls insulin-dependent adipose triglyceride lipase (ATGL) expression and lipolysis in adipocytes. *J. Biol. Chem.* **284**, 13296–13300 (2009).
- Wang, Y., Viscarra, J., Kim, S.-J. & Sul, H. S. Transcriptional regulation of hepatic lipogenesis. *Nat. Rev. Mol. Cell Biol.* **16**, 678–689 (2015).
- Fougerat, A. et al. ATGL-dependent white adipose tissue lipolysis controls hepatocyte PPAR α activity. *Cell Rep.* **39**, 110910 (2022).
- Anthonsen, M. W., Rönstrand, L., Wernstedt, C., Degerman, E. & Holm, C. Identification of novel phosphorylation sites in hormone-sensitive lipase that are phosphorylated in response to isoproterenol and govern activation properties in vitro. *J. Biol. Chem.* **273**, 215–221 (1998).
- Kitamura, T. et al. Insulin-induced phosphorylation and activation of cyclic nucleotide phosphodiesterase 3B by the serine-threonine kinase Akt. *Mol. Cell Biol.* **19**, 6286–6296 (1999).
- Strålfors, P. & Honnor, R. C. Insulin-induced dephosphorylation of hormone-sensitive lipase. *Eur. J. Biochem.* **182**, 379–385 (1989).
- Albert, J. S. et al. Null mutation in hormone-sensitive lipase gene and risk of type 2 diabetes. *N. Engl. J. Med.* **370**, 2307–2315 (2014).
- Xia, B. et al. Adipose tissue deficiency of hormone-sensitive lipase causes fatty liver in mice. *PLoS Genet.* **13**, e1007110 (2017).
- Haemmerle, G. et al. Defective lipolysis and altered energy metabolism in mice lacking adipose triglyceride lipase. *Science* **312**, 734–737 (2006).
- Fischer, J. et al. The gene encoding adipose triglyceride lipase (PNPLA2) is mutated in neutral lipid storage disease with myopathy. *Nat. Genet.* **39**, 28–30 (2007).
- Wu, J. W. et al. Deficiency of liver adipose triglyceride lipase in mice causes progressive hepatic steatosis. *Hepatology* **54**, 122–132 (2011).
- Schoiswohl, G. et al. Impact of reduced ATGL-mediated adipocyte lipolysis on obesity-associated insulin resistance and inflammation in male mice. *Endocrinology* **156**, 3610–3624 (2015).
- Perry, R. J. et al. Glucagon stimulates gluconeogenesis by INSP3R1-mediated hepatic lipolysis. *Nature* **579**, 279–283 (2020). 1–5.

19. Pagnon, J. et al. Identification and functional characterization of protein kinase A phosphorylation sites in the major lipolytic protein, adipose triglyceride lipase. *Endocrinology* **153**, 4278–4289 (2012).
20. Ding, L. et al. Peroxisomal β -oxidation acts as a sensor for intracellular fatty acids and regulates lipolysis. *Nat. Metab.* **3**, 1648–1661 (2021). 1–14.
21. Ghosh, M. et al. Ubiquitin ligase COP1 controls hepatic fat metabolism by targeting ATGL for degradation. *Diabetes* **65**, 3561–3572 (2016).
22. Posor, Y., Jang, W. & Haucke, V. Phosphoinositides as membrane organizers. *Nat. Rev. Mol. Cell Biol.* **23**, 797–816 (2022).
23. Chen, J. & Chen, Z. J. PtdIns4P on dispersed *trans*-Golgi network mediates NLRP3 inflammasome activation. *Nature* **564**, 71–76 (2018).
24. Kopp, Y. et al. CHIP as a membrane-shuttling proteostasis sensor. *eLife* **6**, e29388 (2017).
25. Miao, G., Zhang, Y., Chen, D. & Zhang, H. The ER-localized transmembrane protein TMEM39A/SUSR2 regulates autophagy by controlling the trafficking of the PtdIns(4)P phosphatase SAC1. *Mol. Cell* **77**, 618–632.e5 (2020).
26. Blagoveshchenskaya, A. et al. Integration of Golgi trafficking and growth factor signaling by the lipid phosphatase SAC1. *J. Cell Biol.* **180**, 803–812 (2008).
27. Kim, J. et al. Grasp55^{-/-} mice display impaired fat absorption and resistance to high-fat diet-induced obesity. *Nat. Commun.* **11**, 1–17 (2020).
28. Soni, K. G. et al. Coatamer-dependent protein delivery to lipid droplets. *J. Cell Sci.* **122**, 1834–1841 (2009).
29. Zewe, J. P., Wills, R. C., Sangappa, S., Goulden, B. D. & Hammond, G. R. SAC1 degrades its lipid substrate PtdIns4P in the endoplasmic reticulum to maintain a steep chemical gradient with donor membranes. *eLife* **7**, e35588 (2018).
30. Pohl, C. & Dikic, I. Cellular quality control by the ubiquitin–proteasome system and autophagy. *Science* **366**, 818–822 (2019).
31. Angers, A., Ramjaun, A. R. & McPherson, P. S. The HECT domain ligase Itch ubiquitinates endophilin and localizes to the *trans*-Golgi network and endosomal system. *J. Biol. Chem.* **279**, 11471–11479 (2004).
32. Eisenberg-Lerner, A. et al. Golgi organization is regulated by proteasomal degradation. *Nat. Commun.* **11**, 1–14 (2020).
33. Lee, W. Y. et al. The ubiquitin ligase CBLC maintains the network organization of the Golgi apparatus. *PLoS ONE* **10**, e0138789 (2015).
34. Otten, E. G. et al. Ubiquitylation of lipopolysaccharide by RNF213 during bacterial infection. *Nature* **594**, 111–116 (2021). 1–6.
35. Venditti, R. et al. The activity of Sac1 across ER–TGN contact sites requires the four-phosphate-adaptor-protein-1. *J. Cell Biol.* **218**, 783–797 (2019).
36. Arai, T. et al. Targeted disruption of p185/Cul7 gene results in abnormal vascular morphogenesis. *Proc. Natl Acad. Sci. USA* **100**, 9855–9860 (2003).
37. Tsutsumi, T., Kuwabara, H., Arai, T., Xiao, Y. & DeCaprio, J. A. Disruption of the Fbxw8 gene results in pre- and postnatal growth retardation in mice. *Mol. Cell Biol.* **28**, 743–751 (2008).
38. Litterman, N. et al. An OBSL1-Cul7Fbxw8 ubiquitin ligase signaling mechanism regulates Golgi morphology and dendrite patterning. *PLoS Biol.* **9**, e1001060 (2011).
39. Reid, B. N. et al. Hepatic overexpression of hormone-sensitive lipase and adipose triglyceride lipase promotes fatty acid oxidation, stimulates direct release of free fatty acids, and ameliorates steatosis. *J. Biol. Chem.* **283**, 13087–13099 (2008).
40. Liu, Y. et al. The Sac1 phosphoinositide phosphatase regulates Golgi membrane morphology and mitotic spindle organization in mammals. *MBoC* **19**, 3080–3096 (2008).
41. Reuberson, J. et al. Discovery of a potent, orally bioavailable PI4KIII β inhibitor (UCB9608) able to significantly prolong allogeneic organ engraftment in vivo. *J. Med. Chem.* **61**, 6705–6723 (2018).
42. Ahmadian, M. et al. Adipose overexpression of desnutrin promotes fatty acid use and attenuates diet-induced obesity. *Diabetes* **58**, 855–866 (2009).
43. Morrow, M. R. et al. Inhibition of ATP-citrate lyase improves MASH, liver fibrosis, and dyslipidemia. *Cell Metab.* **34**, 919–936.e8 (2022).
44. Clavien, P.-A. et al. Transplantation of a human liver following 3 days of ex situ normothermic preservation. *Nat. Biotechnol.* **40**, 1610–1616 (2022).
45. Valentine, J. M. et al. β 3-Adrenergic receptor downregulation leads to adipocyte catecholamine resistance in obesity. *J. Clin. Invest.* **132**, e153357 (2022).
46. Violin, J. D. et al. β 2-Adrenergic receptor signaling and desensitization elucidated by quantitative modeling of real time cAMP dynamics. *J. Biol. Chem.* **283**, 2949–2961 (2008).
47. Xu, X. et al. The CUL7 E3 ubiquitin ligase targets insulin receptor substrate 1 for ubiquitin-dependent degradation. *Mol. Cell* **30**, 403–414 (2008).
48. Rambold, A. S., Cohen, S. & Lippincott-Schwartz, J. Fatty acid trafficking in starved cells: regulation by lipid droplet lipolysis, autophagy, and mitochondrial fusion dynamics. *Dev. Cell* **32**, 678–692 (2015).
49. Kaushik, S. & Cuervo, A. M. Degradation of lipid droplet-associated proteins by chaperone-mediated autophagy facilitates lipolysis. *Nat. Cell Biol.* **17**, 759–770 (2015).
50. Loomba, R., Friedman, S. L. & Shulman, G. I. Mechanisms and disease consequences of nonalcoholic fatty liver disease. *Cell* **184**, 2537–2564 (2021).
51. Nielsen, S., Guo, Z., Johnson, C. M., Hensrud, D. D. & Jensen, M. D. Splanchnic lipolysis in human obesity. *J. Clin. Invest.* **113**, 1582–1588 (2004).
52. Mridha, A. R. et al. NLRP3 inflammasome blockade reduces liver inflammation and fibrosis in experimental MASH in mice. *J. Hepatol.* **66**, 1037–1046 (2017).
53. Omari, S. et al. Noncanonical autophagy at ER exit sites regulates procollagen turnover. *Proc. Natl Acad. Sci. USA* **115**, E10099–E10108 (2018).
54. Kim, C.-W. et al. Acetyl CoA carboxylase inhibition reduces hepatic steatosis but elevates plasma triglycerides in mice and humans: a bedside to bench investigation. *Cell Metab.* **26**, 394–406.e6 (2017).

Publisher's note Springer Nature remains neutral with regard to jurisdictional claims in published maps and institutional affiliations.

Open Access This article is licensed under a Creative Commons Attribution 4.0 International License, which permits use, sharing, adaptation, distribution and reproduction in any medium or format, as long as you give appropriate credit to the original author(s) and the source, provide a link to the Creative Commons licence, and indicate if changes were made. The images or other third party material in this article are included in the article's Creative Commons licence, unless indicated otherwise in a credit line to the material. If material is not included in the article's Creative Commons licence and your intended use is not permitted by statutory regulation or exceeds the permitted use, you will need to obtain permission directly from the copyright holder. To view a copy of this licence, visit <http://creativecommons.org/licenses/by/4.0/>.

© The Author(s) 2024

¹Institute of Food, Nutrition and Health, ETH Zürich, Schwerzenbach, Switzerland. ²Macromolecular Engineering Laboratory, Institute of Energy and Process Engineering, ETH Zürich, Zurich, Switzerland. ³Interdisciplinary Research Center on Biology and Chemistry, Shanghai Institute of Organic Chemistry, Chinese Academy of Sciences, Shanghai, China. ⁴Department of Surgery and Transplantation, University of Zurich, Zurich, Switzerland. ⁵Biomedical Research Center, Slovak Academy of Sciences, Bratislava, Slovakia. ⁶Department of Pharmacy, the Sixth Affiliated Hospital, Sun Yat-sen University, Guangzhou, China. ⁷Wyss Zurich Translational Center, ETH Zurich and University of Zurich, Zurich, Switzerland. ✉e-mail: christian-wolfrum@ethz.ch

Methods

Human adipose tissues were obtained from EHC study, which was approved by the by the Local Ethics Committee (Bratislava, Slovakia) and conforms to the ethical guidelines of the 2000 Helsinki declaration. The discarded human liver grafts were from all Swiss transplant centres, which was approved by local authorities (Kantonale Ethik Kommission Zürich KEK Nr. 2017-000412). All animal experiments were approved by the Veterinary office of the Canton of Zurich or Institutional Animal Care and Use Committee of Sun Yat-sen University.

EHC study

All study participants provided witnessed written informed consent before entering the study. Briefly, human insulin (Actrapid 100 IU ml⁻¹, Novo Nordisk) was infused into the antecubital vein in a primed continuous fashion at the dose of 1 mU kg⁻¹ min⁻¹. Blood glucose was measured in the samples from the contralateral antecubital vein in 5 min intervals and maintained at euglycaemia (5.0 ± 0.25 mM) using variable infusion rate of 20% glucose. The whole-body insulin sensitivity (*M* value) was calculated from the steady-state plasma glucose infusion rate required to maintain euglycaemia and expressed per kg BW per minute, normalized to the steady-state insulinemia. Subcutaneous AT samples were taken by needle biopsy from abdominal region in the basal fasted state as well as during the steady state of EHC. Twenty-four middle-aged sedentary men (age 35.5 ± 1.5 years, body mass index 28.9 ± 1.1 kg m⁻², adiposity 25.7 ± 1.6%) were assigned to insulin-sensitive (*n* = 16, *M* value 0.14 ± 0.02 mg per kg BW per minute per μU insulin per millilitre) and insulin-resistant (*n* = 8, *M* value 0.04 ± 0.01 mg per kg BW per minute per μU insulin per millilitre) subgroups according to their insulin sensitivity index.

Human liver perfusion

The graft had an initial weight of 2,740 g (with gallbladder) before perfusion and was diagnosed with 15% macrovesicular steatosis by the pathological department of the University Hospital Zürich. The liver was procured with a total ischaemia time of 40 min after circulatory death of the donor. It was flushed with IGL-1 solution and perfused for 2 h with Belzer MPS at 8 °C. The infrahepatic vena cava was closed with a suture, and the hepatic artery, portal vein, suprahepatic vena cava and common bile duct were cannulated with steel cannulas. The graft was subsequently perfused with whole blood and a custom built normothermic perfusion machine⁵⁵. Hepatic arterial pressure was controlled to 80/50 mmHg, allowing for an average flow of 0.25 l min⁻¹. Epoprostenol was automatically infused to keep arterial flow stable. Oxygenation was automatically controlled with a setpoint partial pressure of oxygen equal to 12 kPa. Portal venous flow was controlled to 1 l min⁻¹, resulting in a pressure of 2 mmHg on average. Further, oxygenation of portal blood was automatically regulated to achieve 65% saturation in the vena cava. Use of an electric pinch valve further allowed for pressure regulation in the vena cava, keeping a constant pressure of 0 mmHg. Glucose levels were automatically controlled by using a real-time glucose sensor (CCIT) and automated insulin infusions, keeping glucose levels at 7 mmol l⁻¹ from the second day of perfusion onwards. A dialysis bypass was used to clear waste metabolites and control haematocrit levels by using a fixed dialysate influx rate of 200 ml h⁻¹ and an automatically controlled outflow. After 8 days of perfusion, the liver weight decreased to 1,507 g (without gallbladder) and was sent for pathological examination. The liver graft finally displayed less than 5% macrovesicular steatosis determined by the pathological department of the University Hospital Zürich. Further, two control livers diagnosed with 30% and 50% macrovesicular steatosis grades were perfused for 69 h and 158 h, respectively. Both livers were perfused with the same perfusion device and perfusion protocol but did not receive a daily bolus of UCB9608.

Mouse experiments

Both female and male mice were used in the experiments starting at the age of 8–10 weeks and they were housed two to five littermates per

cage in ventilated cages at standard housing conditions (40% humidity, 22 °C, 12 h reversed light/dark cycle, dark phase starting at 7:00) with NCD (18% protein, 4.5% fibre, 4.5% fat, 6.3% ash, Provimi Kliba SA) and water. C57BL/6N male mice (Charles River Laboratories) were fasted for 24 h or injected with 2-DG (2 g kg⁻¹ BW) for different durations. Female *ROSA26-LSL-spCas9* mice (#024857, JAX) were intravenously injected with various virus pools to express gRNA pools and CAS9 at a dose of 3 × 10¹¹ genome copies per mouse. Two or four weeks later, livers were collected after 6 h fasting for protein and RNA extraction or TG determination, respectively. Also 4 weeks later, the liver-specific *Cul7&Fbxw8* double knockout mice were injected with 2-DG to induce 1 h glucose deprivation before dissection.

To study CUL7 and FBXW8 in MASLD model, male *ROSA26-LSL-spCas9* mice were injected with virus pools and fed a HFD (#3436, Provimi Kliba SA) for 12 weeks, followed by dissection after 6 h fasting. To study P14KB in MASLD model, male *ROSA26-LSL-spCas9* mice were fed in HFD for 12 weeks before induction of P14KB depletion. Mice were fed a HFD for another 8 weeks and dissected after 6 h fasting. Likewise, male C57BL/6N wild-type mice and *Atgl* KO were challenged with HFD for 12 weeks before administration of UCB9608 mixed in HFD (5 mg kg⁻¹) for another 8 weeks. Then the mice were dissected after 6 h fasting.

Atgl floxed mice (#024278, JAX) were crossed with *Albumin-Cre* (#035593, JAX) and *Adip-CreERT2* strains to obtain *Alb-Atgl^{fl/fl}* and *Adip-creERT2-Atgl^{fl/fl}* mice⁵⁶, which deplete ATGL protein in the liver and adipocytes (induced by tamoxifen), respectively. Male mice from both strains were injected with 2-DG to induce glucose deprivation for 6 h before dissection.

2-DG and insulin administration

Wild type C57BL/6N mice were intraperitoneally injected with saline or 2-DG for 5.5 h treatment, followed by insulin treatment (Actrapid, human insulin at dose of 0.75 U kg⁻¹ BW) for 30 min. The mice were then dissected to study the acute anti-lipolytic effect of insulin under the background of glucose deprivation. To study the long-term anti-lipolytic effect of insulin during glucose deprivation, mice were co-administered with 2-DG and insulin for 6 h treatment before dissection.

UCB9608 administration in murine MASH model

To model MASH in murine liver, male C57BL/6N mice were challenged with HFD for 24 weeks in conjunction with 18.9 g l⁻¹ glucose & 23.1 g l⁻¹ fructose-containing drinking water under thermoneutral housing condition (29 °C) before the administration of UCB9608 via diet (15 mg kg⁻¹) for 12 weeks. Then the mice were analysed in EchoMRI for body composition measurement before 6 h fasting, followed by dissection.

Indirect calorimetry

C57BL/6N male mice were fed on HFD mixing with UCB9608 (5 mg kg⁻¹) for 3 weeks before indirect calorimetry measurements were performed with Phenomaster (TSE systems) according to the manufacturer's instructions. The energy expenditure between both groups was analysed via the analysis of covariance method (<https://www.mmpc.org/shared/regression.aspx>)⁵⁷.

Cell culture

iBAs were cultured as described before⁵⁸. Briefly, iBAs were cultured on collagen-coated plates in Dulbecco's modified Eagle medium (DMEM, high glucose) with 10% foetal bovine serum (FBS) plus 1% Pen/Strep. Once pre-adipocytes reached confluence, adipogenesis was induced by differentiation medium containing 3-Isobutyl-1-methylxanthine (500 μM), dexamethasone (1 μM), insulin (20 nM), T3 (1 nM) and indomethacin (125 μM) for 2 days. Afterwards, iBAs were refreshed with maintenance medium containing insulin (20 nM), T3 (1 nM). Differentiated iBAs were re-seeded at day 5, and all the experiments were routinely performed at day 9. Lipofectamine RNAiMAX reagent-mediated siRNA (100 nM) delivery was performed to knock down target genes for 72 h in iBAs after one

day recovery from replating. To deprive glucose, we either added 2-DG or refreshed cells with DMEM containing different glucose concentrations prepared from the DMEM (Gibco, A1443001) with the same concentration of insulin and T3 as the maintenance medium.

HEK293T (ab255449, Abcam) and HEK293-AAV cells (AAV-100, Cell Biolabs) were cultured in DMEM (high glucose) with 10% FBS and 1% Pen/Strep. HEK293-AAV cells were used for imaging, whereas HEK293T cells were adopted for the rest of the work. We used Lipofectamine 2000 to transiently overexpress EGFP-P4M, EGFP-SACM1L, EGFP-SACM1LK2A, ATGL-FLAG, ATGL-HA, ATGLK0-HA and FBXW8-FLAG in the HEK cells for diverse experimental designs. To image LDs, HEK293-AAV cells were induced by 200 μ M OA (O1008 from Sigma) conjugated to bovine serum albumin (BSA, A6003, Sigma) for 24 h before 4% paraformaldehyde (PFA) fixation. Afterwards, cells were stained by BODIPY 493/503 and Hoechst 33342. In other conditions, HEK cells were not treated with OA-containing medium.

HepG2 cells (HB-8065, ATCC) were cultured in RPMI medium with 10% FBS and 1% Pen/Strep on collagen-coated plates. Lipofectamine RNAiMAX reagent-mediated siRNAs (100 nM) were delivered to cells at the suspended state for 48 h. It is not necessary to induce LDs via OA addition in the HepG2 cells before LD imaging. We treated HepG2 cells with 10 μ M PF-04620110 & PF-06424439 for 48 h or with 5 μ g ml⁻¹ BFA (B5936, Sigma) for 6 h to deplete LDs and intact Golgi in the HepG2 cells, respectively, before glucose deprivation.

All the cell lines used in this work were regularly tested negative for mycoplasma contamination. All the siRNAs used in these cell lines are listed in Supplementary Table 1.

RNA extraction and qPCR

Total RNA was extracted via TRIzol reagent (Invitrogen) according to the manufacturer's instructions. One microgram of total RNA was used to convert into complementary DNA library by using the High-Capacity cDNA Reverse Transcription Kit (Applied Biosystems, 4368813). Quantitative polymerase chain reaction (qPCR) was performed using KAPA SYBR FAST Universal kit (Roche, KK4618) on ViiA7 (Applied Biosystems), and the relative transcript levels were normalized to *36B4* expression via the $\Delta\Delta$ Ct method. Primer sequences are listed in Supplementary Table 2.

Molecular cloning

Human ATGL-FLAG and ATGLK0-FLAG expression constructs were generated as described previously²⁰. Based on these vectors, we designed primers to replace FLAG with HA tag and insert them into pEGFP-N1-FLAG vector (Addgene, 60360) to obtain ATGL-HA and ATGLK0-HA expression constructs. Human SACM1L and SACM1LK2A coding sequence (CDS) were cloned from mCherry-FKBP-SAC1 (Addgene, 108127) and inserted into pEGFP-C1-FLAG vector (Addgene, 46956) to have EGFP tag in the N-terminus. Human FBXW8-FLAG CDS was cloned from HEK293T cDNA library and inserted into pLenti-CMV-MCS-BSD vector to obtain pLenti-FBXW8-FLAG construct. Human FBXW8 mutant CDS with substitution of lysines and arginines into alanines in the N terminus was ordered from Vectorbuilder, and the CDS was then inserted into pLenti-CMV-MCS-BSD vector to obtain pLenti-FBXW8 mutant-FLAG construct. Scarlet-Giantin CDS was cloned from plasmid pmScarlet-Giantin-C1 (Addgene, 85048) and inserted into pLenti-CMV-MCS-BSD vector to obtain pLenti-Scarlet-Giantin construct. Sequences to transcribe six different gRNAs targeting individual gene were ordered from Microsynth AG and inserted into AAV-U6-TBG-Cre vectors so that AAV-U6-Pi4kb gRNA-TBG-Cre, AAV-U6-Sacm1l gRNA-TBG-Cre, AAV-U6-Cul7 gRNA-TBG-Cre and AAV-U6-Fbxw8 gRNA-TBG-Cre were constructed. All the plasmids for cell culture work were extracted by NucleoBond Xtra-Midi kit (Macherey-Nagel, 740410.100).

Virus packaging and stable cell line construction

For lentivirus packaging, the pLenti-Scarlet-Giantin, pLenti-FBXW8-FLAG or pLenti-FBXW8 mutant-FLAG plasmids were transfected into

HEK293T cells together with pMD2.G (Addgene, 12259) and psPAX2 (Addgene, 12260) by polyethylenimine in OptiMEM medium. The virus-containing medium was collected and concentrated in PEG-it Virus Precipitation Solution (SBI, LV825A-1) according to the manufacturer's instructions. The concentrated lentiviruses and polybrene (Sigma, H9268) were added into HEK cells for later selection by 10 μ g ml⁻¹ blasticidin (ThermoFisher, A1113903).

For AAV8 packaging, the AAV8 serotype helper plasmid (PF0478, PlasmidFactory) and various AAV plasmids were transfected into HEK293-AAV cells via polyethylenimine in OptiMEM medium. The medium was collected for concentration via AAVanced Concentration Reagent (SBI, AAV110A-1) according to the manufacturer's instructions. The titre of concentrated viruses was determined by qPCR based on titre determination protocol from Addgene.

Golgi apparatus and LD extraction

Minute Golgi Apparatus Enrichment Kit (GO-037, Invent Biotechnologies) was used to fractionate Golgi and Golgi-related vesicles according to the manufacturer's instructions. LDs isolation was performed as described previously⁵⁹. Briefly, HepG2 cells were collected in cold phosphate-buffered saline (PBS) and centrifuged at 500g for 10 min to pellet cells that were incubated in cold hypotonic lysis medium (20 mM Tris-HCl pH 7.4 and 1 mM ethylenediaminetetraacetic acid (EDTA)) protease inhibitors (Complete, Roche). After being homogenized in a Dounce, the homogenate was centrifuged at 1,000g for 10 min to collect the supernatant for further ultracentrifugation via hypotonic lysis medium at different sucrose concentrations. The buoyant fractions were collected and finally suspended in 1% sodium dodecyl sulfate containing RIPA buffer for immunoblotting analyses.

Immunoblotting, immunoprecipitation, co-IP and immunofluorescence

Tissues and cell cultures were homogenized in RIPA buffer (50 mM Tris-HCl pH 7.4, 150 mM NaCl, 2 mM EDTA, 1.0% Triton X-100 and 0.5% sodium deoxycholate) with protease inhibitors and phosphatase inhibitors (Halt phosphatase inhibitor cocktail, ThermoFisher). The homogenates were centrifuged at 12,000g for 10 min at 4 °C to collect WCE. The concentration of WCE was determined by DC Protein Assay (Bio-Rad). After boiling the sample with Laemmli buffer at 95 °C for 5 min, equal amount of proteins was loaded and separated on 12% sodium dodecyl sulfate polyacrylamide gel electrophoresis. The proteins were transferred to nitrocellulose membrane and blotted by different antibodies. The primary antibody signal was visualized by horseradish peroxidase-conjugated secondary antibodies (1:5,000, Millipore) and the ImageQuant system (GE Healthcare Life Sciences).

To immunoprecipitate FLAG-tagged ATGL or FBXW8, HEK293T cells were homogenized in RIPA buffer (50 mM Tris-HCl pH 7.4, 150 mM NaCl, 2 mM EDTA and 1.0% Triton X-100) with protease inhibitors and phosphatase inhibitors. The homogenates were centrifuged at 12,000g for 10 min at 4 °C to collect WCE. After three washes with cold RIPA buffer, 20 μ l Anti-FLAG beads (A2220, Sigma) was added to WCE for overnight incubation with rotation at 4 °C. The beads were then washed six times by cold RIPA buffer. The proteins were eluted by boiling the beads at 95 °C for 5 min with 2 \times Laemmli buffer. The eluted protein was then analysed by immunoblotting.

To immunostain ATGL, GM130, CUL7, FBXW8 and FBXW8-FLAG in HEK293-AAV cells or a stable cell line expressing Scarlet-Giantin to visualize Golgi after various treatments, HEK293-AAV cells were fixed by 4% PFA for 20 min and permeabilized by 0.25% PBST (Triton X-100 in PBS) or 20 μ M digitonin in PBS (ATGL immunostaining) for 20 min. After three washes with cold PBS, cells were blocked by 1% BSA for 1 h and incubated with primary antibodies overnight at 4 °C. After three washes with cold PBS, cells were incubated with Alexa Fluor 488 conjugated secondary antibody (1:200, ThermoFisher) for 1 h at room temperature. Finally, cells were stained by Hoechst 33342 to label nuclei after three washes with

PBS to remove residual secondary antibody. We determined the ATGL intensity/Golgi area ratio or FBXW8 intensity/Golgi area ratio to quantify the Golgi ATGL or FBXW8 levels, respectively. Likewise, we used the same procedures to immunostain GM130 in HepG2 cells except for using Alexa Fluor 568 conjugated secondary antibody (1:200, ThermoFisher).

To immunostain ATGL in the iBAT, the tissues were fixed by 4% PFA overnight at 4 °C after dissection. Then 10% sucrose and 30% sucrose solution were used to dehydrate samples before cryosection at 15 µm. The slides were washed once in PBS for 5 min and 3 washes in 0.1% PBST before blocking with 10% normal donkey serum diluted in PBST for 1 h. Afterwards, ATGL antibody (1:100, Cell Signaling) was diluted in blocking solution for overnight incubation at 4 °C. The residual antibody was washed with PBST three times before application of Alexa Fluor 568 conjugated secondary antibody (1:200 in 5% normal donkey serum, ThermoFisher) for 1 h. At last, the slides were treated with mounting solution after three washes with PBST.

The pictures were all obtained by Olympus FluoView 3000 confocal microscope and processed by ImageJ.

PtdIns4P determination

HEK293-AAV cells were transfected with Scarlet-Giantin and EGFP-P4M and glucose-deprived. The cells were live-imaged, and the Golgi PtdIns4P levels were determined as Golgi GFP intensity/cytosolic GFP intensity ratio in the individual cells. To immunostain cellular PtdIns4P at different conditions, Scarlet-Giantin expressing HEK293-AAV cells were fixed by 4% PFA for 15 min and washed three times with PBS containing 50 mM NH₄Cl, followed by permeabilization for 5 min with 20 µM digitonin in PBS. After being washed three times with PBS, cells were blocked with 5% normal goat serum (NGS) in PBS with 50 mM NH₄Cl for 1 h at room temperature. Primary anti-PtdIns4P antibody (1:100 in 5% NGS; Echelon Biosciences) was applied to cells overnight at 4 °C. Alexa Fluor 488 conjugated secondary antibody (1:200 in 5% NGS, ThermoFisher) was replaced with three washes before capturing images under microscope. We determined the PtdIns4P intensity/Golgi area ratio to quantify the Golgi PtdIns4P. PtdIns4P Mass ELISA Assay Kit (K-4000E, Echelon Biosciences) was used to determine the total mass of PtdIns4P from HEK293T cells according to the manufacturer's instructions.

Membrane Lipid Strip assay, PIP Strip assay and pull-down by PtdIns4P agarose beads

FLAG Purification Kit (CELLMM2, Sigma) was used to purify wild-type and mutant FBXW8 from established HEK293T stable cell lines according to the manufacturer's instructions. The eluted proteins were filtered and concentrated using a 10-kDa cut-off concentrator (Pierce, 88513).

Membrane Lipid Strip (P-6002, Echelon Biosciences) and PIP Strip (P-6001, Echelon Biosciences) were used to perform binding assays between recombinant proteins and lipids as described previously²³. PtdIns4P-conjugated beads (P-B004, Echelon Biosciences), phosphatidylcholine-conjugated beads (P-BOPC, Echelon Biosciences) and control beads (P-B000, Echelon Biosciences) were used to pull down purified recombinant proteins according to the manufacturer's instructions. Briefly, 100 µl slurry was pelleted by centrifugation at low speed and then resuspended in 300 µl wash-binding buffer (10 mM HEPES, pH 7.4, 150 mM NaCl and 0.25% Igepal). Ten micrograms recombinant wild-type and mutant FBXW8 were added for 3 h incubation. The beads were pelleted and washed with wash-binding buffer six times. At last, the proteins were eluted by boiling the beads at 95 °C for 5 min with 2× Lämmeli buffer and analysed by immunoblotting.

Lipolysis measurement

Day 9 iBAs were washed with pre-warmed PBS and then starved by phenol-red-free DMEM (low glucose) with 1% FA-free BSA for 2 h. After medium collection, NEFA release was measured with an NEFA assay kit (Wako NEFA kit) and normalized to total protein mass. Similarly, the

dialysates from liver graft during ex vivo perfusion were measured to determine NEFA levels. All the photometric and fluorometric measurements were performed via Synergy Gen5 Platereader.

Measurement of insulin, glucose, FFA, TG and ALT and AST activity in the plasma

Plasma insulin levels were determined via Ultra-sensitive Mouse Insulin ELISA Kit (Crystal Chem, 90080). Plasma glucose levels were determined via glucose assay kit (Sigma, MAK263). Plasma FFA levels were determined via NEFA assay kit (Wako NEFA kit). Plasma TG levels were determined via TG assay kit (Roche Trig/GB reagent). Alanine transaminase (ALT) (MAK052, Sigma) and aspartate aminotransferase (AST) (MAK055, Sigma) assay kits were used to determine ALT and AST activity. All the assays were performed according to the manufacturers' instructions.

Determination of hepatic glucose, glucose-6-phosphate and glyceraldehyde 3-phosphate levels

Liver pieces were homogenized in two volumes of ice-cold PBS. The homogenates were centrifuged at 13,000g for 10 min to collect supernatant, which was deproteinized with a 10 kDa molecular weight cut-off spin filter (Pierce, 88513). One microlitre sample was used to measure glucose levels via Glucose Assay Kit (Sigma, MAK263). Ten microlitres sample was used to measure glucose-6-phosphate levels via Glucose-6-Phosphate Assay Kit (Sigma, MAK014) or to measure glyceraldehyde 3-phosphate levels via Glyceraldehyde 3-Phosphate Assay Kit (Abcam, ab273344). All the concentrations were normalized to the protein concentration.

Liver FA oxidation and TG determination

We measured liver FAO as described previously^{20,60}. To measure TG levels, weight of liver pieces (50–100 mg) was recorded before homogenization by 1 ml isopropanol per 50 mg tissue. The homogenates were incubated with rotating before centrifugation at 2,000g for 10 min to collect supernatant. The TG levels were determined via Roche Trig/GB reagent.

Histologic staining

Livers were fixed in 4% PFA for 24 h directly after tissue collection. To perform haematoxylin and eosin (H&E) staining, liver pieces were transferred to 65% ethanol and embedded in paraffin in tissue processing machine and embedding machine, followed by section at 10 µm and staining using the standard protocol. To perform Oil Red O (ORO) staining, the fixed livers were dehydrated before cryosection at 20 µm and staining via ORO solution (O1516, Sigma).

For MASH cohort, livers were fixed with 4% PFA for 24 h at 4 °C. The samples were sent to the University of Zurich for histologic analyses. Briefly, liver tissues were dehydrated and embedded in paraffin before section at 3 µm, followed by staining with H&E and Gomori Green Trichrome or anti-cleaved Caspase-3 after antigen retrieval. The images were captured by digital slide scanners, and the grade of steatosis, ballooning, inflammation and fibrosis were quantified via the MASH Clinical Research Network Scoring System⁶¹. For ORO staining, the fixed samples were cryosectioned, and the slides were stained via ORO solution and eosin.

Statistics and reproducibility

For in vivo studies, littermates were randomly assigned to treatment groups for all the experiments, but no randomization was performed for in vitro experiments. Sample size was determined on the basis of previous experiments, and the animal numbers used in the experiments are all indicated in the corresponding figure legends. No data were excluded from the analyses, and the investigators were not blinded to allocation during experiments and outcome assessment. For cell culture experiments, biological replicates were no less than three (shown as *n* in the figure legend), and all the cell culture experiments were performed with two to three technical replicates for RNA and protein analysis. Results

are represented as mean \pm s.e.m. when it is not indicated specifically. Two-tailed unpaired or paired Student's *t*-test was applied on comparison of two groups when the data are in normal distribution, otherwise Mann–Whitney test or Wilcoxon test was adopted. Analysis of variance (ANOVA) was applied on comparisons of multiple groups when the data are in normal distribution, otherwise Kruskal–Wallis test was adopted. All statistical analyses were performed using GraphPad Prism 9. Statistical differences are indicated as exact *P* value or non-significant (n.s.).

Reporting summary

Further information on research design is available in the Nature Portfolio Reporting Summary linked to this article.

Data availability

Source data are provided with this paper. All other data supporting the findings of this study are available from the corresponding author on reasonable request.

References

55. Eshmuminov, D. et al. An integrated perfusion machine preserves injured human livers for 1 week. *Nat. Biotechnol.* **38**, 189–198 (2020).
56. Sitnick, M. T. et al. Skeletal muscle triacylglycerol hydrolysis does not influence metabolic complications of obesity. *Diabetes* **62**, 3350–3361 (2013).
57. MMPC energy expenditure analysis page. *Mouse Metabolic Phenotyping Centers* <https://www.mmpc.org/shared/regression.aspx>
58. Perdikari, A. et al. A high-throughput, image-based screen to identify kinases involved in brown adipocyte development. *Sci. Signal.* **10**, eaaf5357 (2017).
59. Bersuker, K. et al. A proximity labeling strategy provides insights into the composition and dynamics of lipid droplet proteomes. *Dev. Cell* **44**, 97–112.e7 (2018).
60. He, A. et al. Acetyl-CoA derived from hepatic peroxisomal β -oxidation inhibits autophagy and promotes steatosis via mTORC1 activation. *Mol. Cell* **79**, 30–42.e4 (2020).
61. Kleiner, D. E. et al. Design and validation of a histological scoring system for nonalcoholic fatty liver disease. *Hepatology* **41**, 1313–1321 (2005).

Acknowledgements

We are grateful to the organ donors and their families for their support which allowed for the experiments with discarded human liver grafts. We thank the team members of Liver4Life, a Wyss Zurich Translational Center project, for their support during the human liver perfusion. We thank X. Lou for the assistance of histological scoring of MASH liver images. We further thank C. Le Foll for supporting preliminary perfusion experiments with rodent livers. The schemas shown in Figs. 5i and 7m were created with BioRender.com. The work was supported by the Swiss National Science Foundation (SNSF 200377 to C.Wo.).

Author contributions

L.D., F.H., M.W.T. and C. Wo. designed the study; L.D. and C. Wo. supervised the experiments; L.D., F.H., F.L., W.Y., J.B., K.W., M.P., M.K., M.B., B.U., C. Wu, T.W. and M.G. performed the experiments; L.D. and C. Wo. wrote the paper; all authors reviewed and edited the paper.

Funding

Open access funding provided by Swiss Federal Institute of Technology Zurich.

Competing interests

The authors declare no competing interests.

Additional information

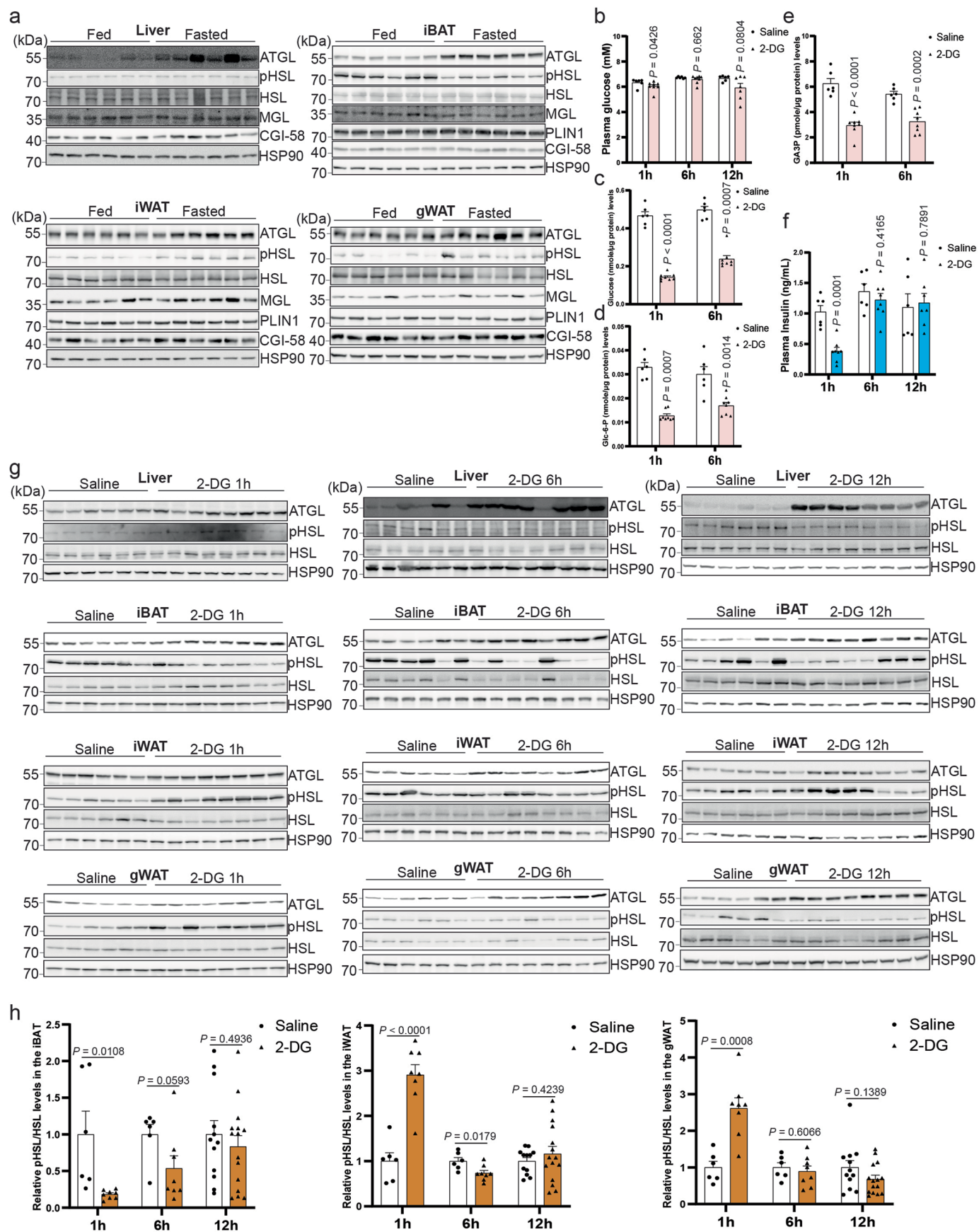
Extended data is available for this paper at <https://doi.org/10.1038/s41556-024-01386-y>.

Supplementary information The online version contains supplementary material available at <https://doi.org/10.1038/s41556-024-01386-y>.

Correspondence and requests for materials should be addressed to Christian Wolfrum.

Peer review information *Nature Cell Biology* thanks Antonella De Matteis, Douglas Mashek and Matthew Watt for their contribution to the peer review of this work.

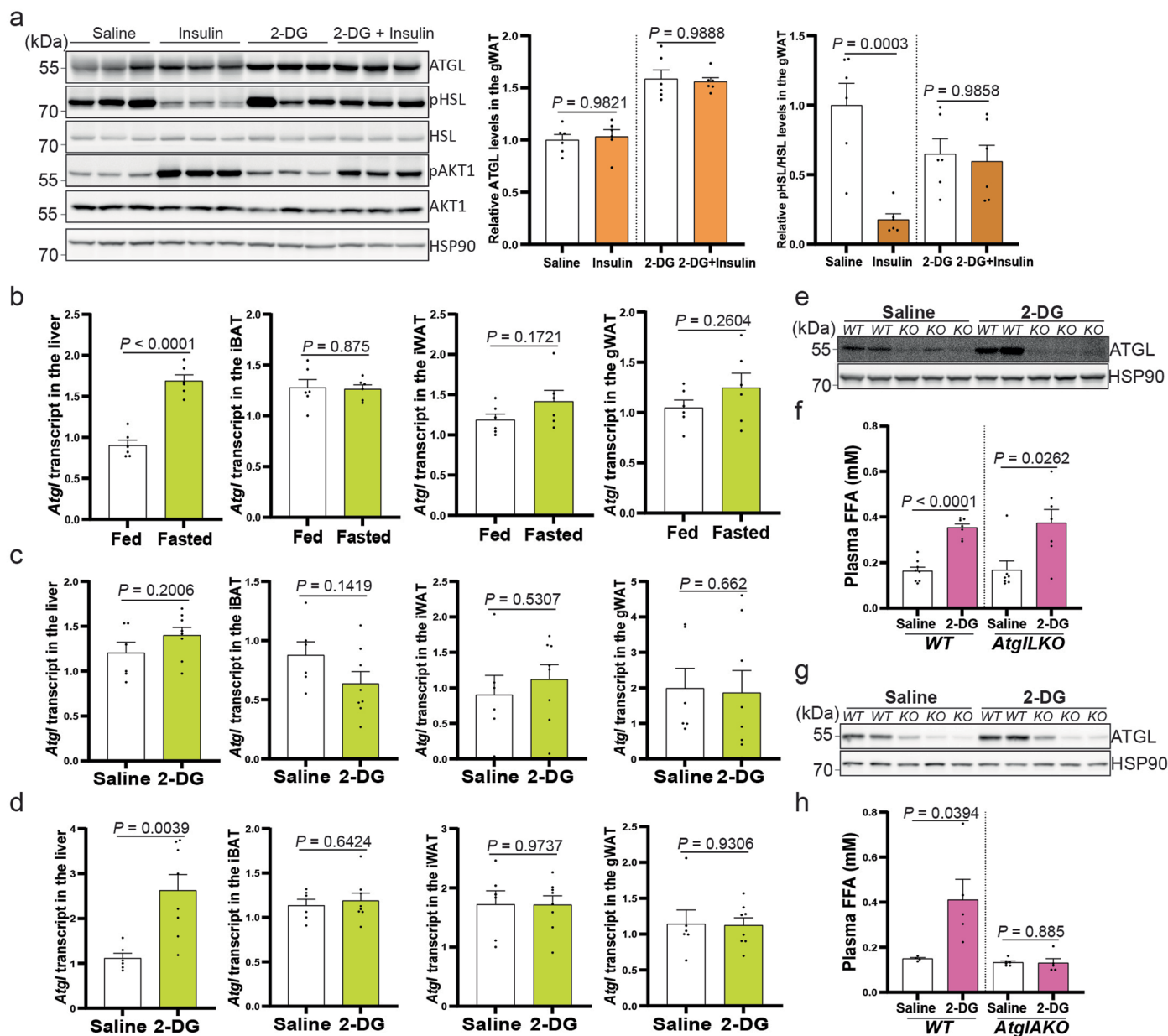
Reprints and permissions information is available at www.nature.com/reprints.



Extended Data Fig. 1 | See next page for caption.

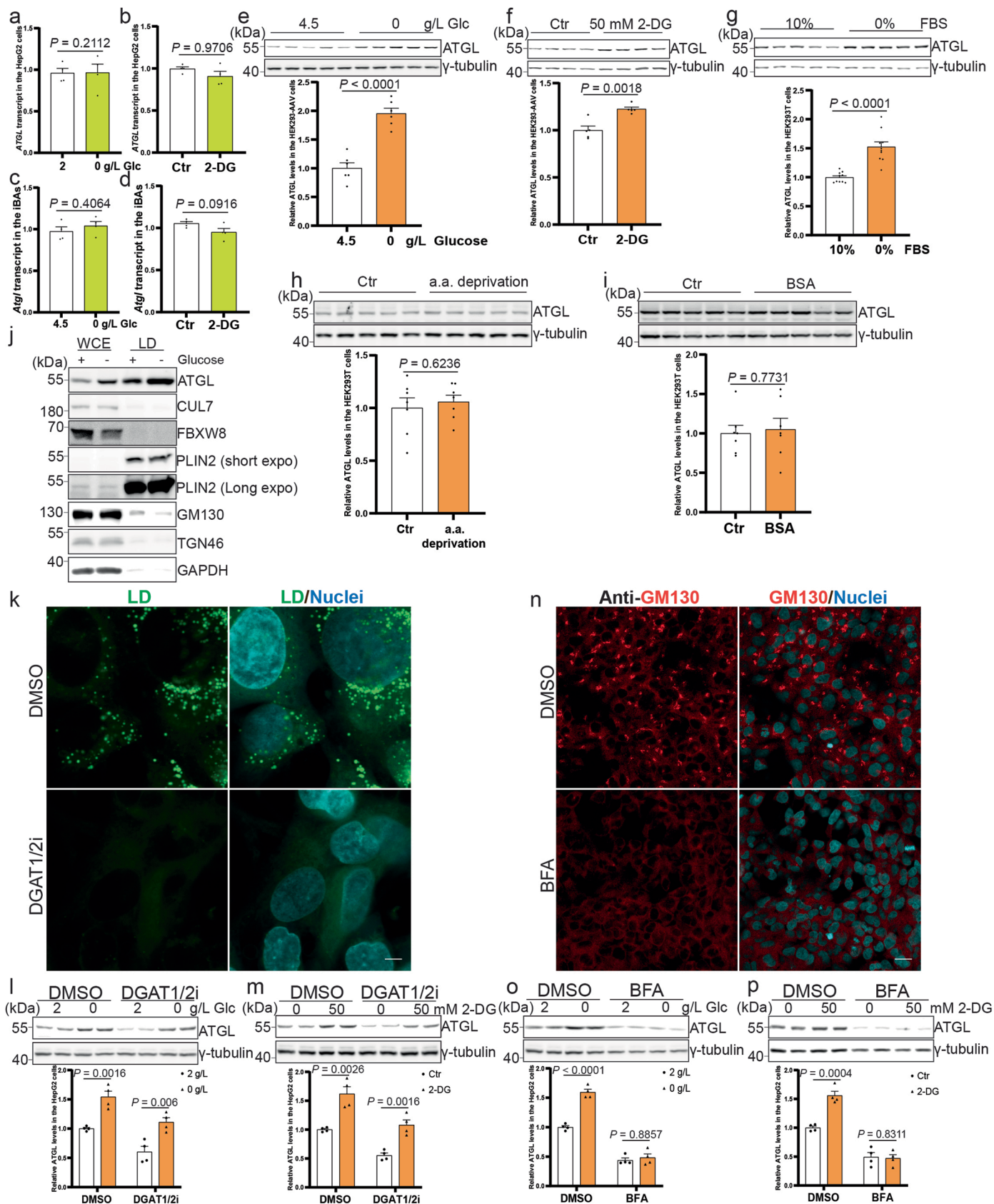
Extended Data Fig. 1 | ATGL-driven lipolysis is increased in the liver and adipose depots from fasted and glucose-deprived mice. (a) Immunoblots of ATGL, HSL^{Ser660ph}, HSL, MGL, PLIN1, CGI-58 and HSP90 in the liver and adipose depots from fed and fasted mice. (b) Plasma glucose levels in the wild-type mice 1 h, 6 h and 12 h after 2-DG (2 g/kg BW) administration (1 h and 6 h, n = 6 mice for saline and 8 mice for 2-DG group; 12 h, n = 6 mice for saline and 7 mice for 2-DG group). (c–e) Levels of glucose and glucose derivatives (glucose-6-p and GA3P) in the livers of wild-type mice collected 1 h and 6 h after 2-DG (2 g/kg BW) administration (n = 6 mice for saline and 8 mice for 2-DG group). (f) Plasma insulin levels in the wild-type mice 1 h, 6 h and 12 h after 2-DG (2 g/kg BW) administration (1 h and 6 h, n = 6 mice for saline and 8 mice for 2-DG group;

12 h, n = 6 mice for saline and 7 mice for 2-DG group). (g) Immunoblots of ATGL, HSL^{Ser660ph}, HSL and HSP90 in the liver and adipose depots collected 1 h, 6 h and 12 h after 2-DG (2 g/kg BW) administration. (h) Quantification of HSL^{Ser660ph} levels in the adipose depots collected 1 h, 6 h and 12 h after 2-DG (2 g/kg BW) administration (1 h and 6 h, n = 6 mice for saline and 8 mice for 2-DG group; 12 h, n = 12 mice for saline and 15 mice for 2-DG group). Results are shown as mean \pm s.e.m. and analyzed using two-tailed unpaired *t*-test (b (12 h), c (1 h), d (6 h), e, f and h (1 h and 12 h in iBAT, iWAT and gWAT)) and two-tailed Mann-Whitney test (b (1 h and 6 h), c (6 h), d (1 h) and h (6 h in iBAT)). Source numerical data and unprocessed blots are available in source data.



Extended Data Fig. 2 | Glucose deprivation elevates systemic lipolysis via upregulating ATGL in the adipose depots independently of transcriptional changes. (a) Immunoblots of ATGL, HSL^{Ser60ph}, HSL, AKT1, AKT1^{Ser473ph} and HSP90 in the gWAT from wild-type mice after 2-DG (2 g/kg BW) treatment for 5.5 h, followed by insulin (0.75 U/kg BW) administration for 30 minutes (n = 6 mice per group). (b) Quantification of *Atgl* transcript levels in the liver and adipose depots from fasted mice via qPCR (n = 6 mice per group). (c) Quantification of *Atgl* transcript levels in the liver and adipose depots collected 1 h after 2-DG (2 g/kg BW) administration (n = 6 mice for saline and 8 mice for 2-DG group). (d) Quantification of *Atgl* transcript levels in the liver and adipose depots collected 6 h after 2-DG (2 g/kg BW) administration (n = 6 mice for saline and

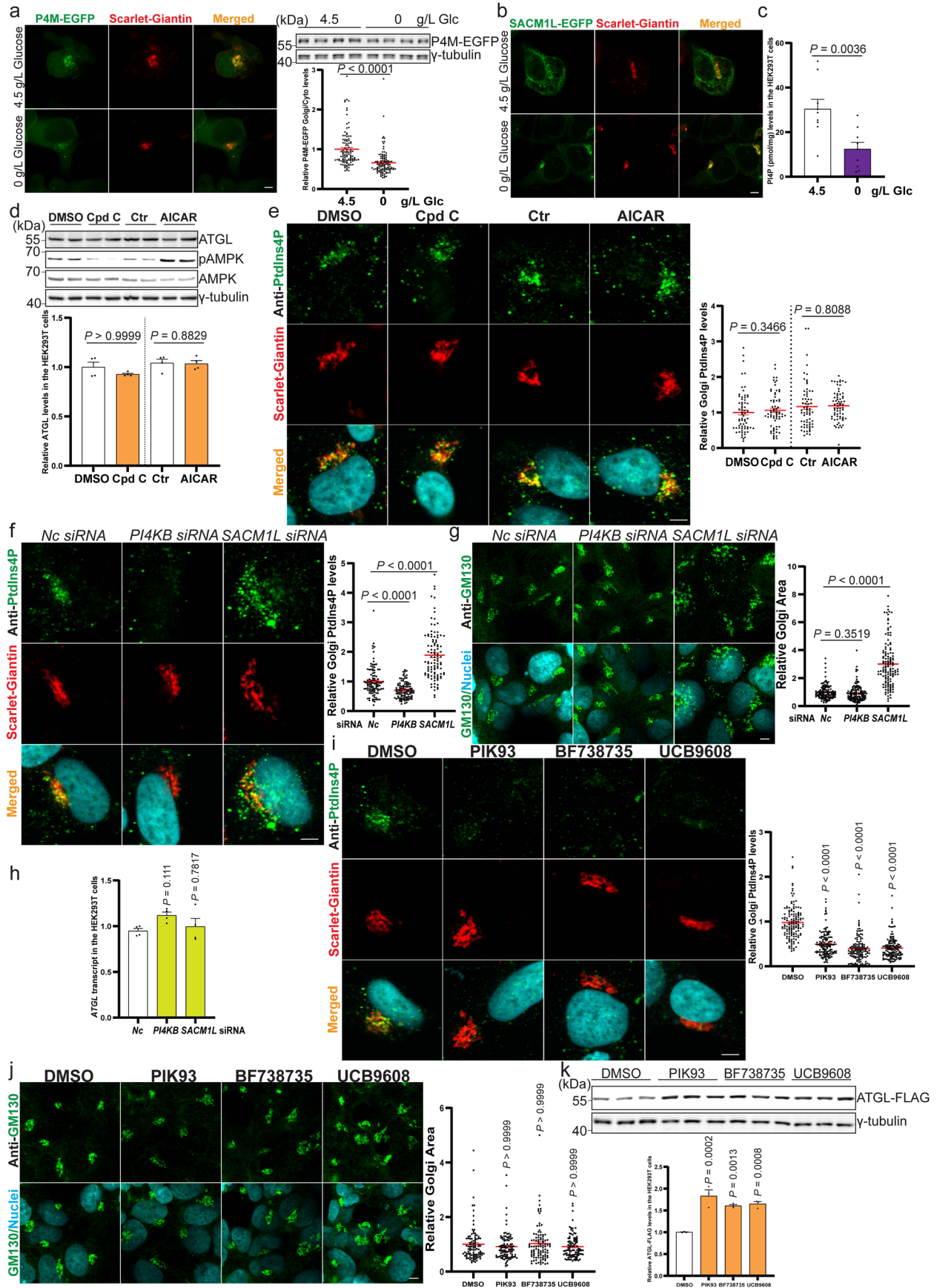
8 mice for 2-DG group). (e–f) Immunoblot of ATGL in the liver and determination of plasma FFA levels in liver-specific *Atgl* knockout mice (*AtgILKO*) 6 h after 2-DG (2 g/kg BW) administration (WT: n = 8 mice for saline and 7 mice for 2-DG group; *AtgILKO* mice: n = 7 mice per group). (g–h) Immunoblot of ATGL in the iBAT and determination of plasma FFA levels in adipose tissue-specific *Atgl* knockout mice (*AtgIAKO*) 6 h after 2-DG (2 g/kg BW) administration (WT: n = 4 mice for saline and 5 mice for 2-DG group; *AtgIAKO*: n = 6 mice for saline and 5 mice for 2-DG group). Results are shown as mean ± s.e.m. and analyzed using two-tailed unpaired *t*-test (b, c (liver, iBAT and iWAT), d, f (WT) and h), two-tailed Mann-Whitney test (c (gWAT) and f (*AtgILKO*)) and one-way ANOVA method with Tukey correction (a). Source numerical data and unprocessed blots are available in source data.



Extended Data Fig. 3 | See next page for caption.

Extended Data Fig. 3 | ATGL protein is stabilized in various cell types treated with glucose or serum deprivation. (a–b) Quantification of *ATGL* transcript levels in the HepG2 cells 6 h after glucose withdrawal or 50 mM 2-DG treatment (n = 4 independent experiments per group). (c, d) Quantification of *Atgl* transcript levels in the iBAs 24 h after glucose withdrawal and 100 mM 2-DG treatment (n = 4 independent experiments per group). (e) Immunoblot of ATGL in the HEK293-AAV cells 6 h after glucose withdrawal (n = 6 independent experiments per group). (f) Immunoblot of ATGL in the HEK293-AAV cells 12 h after treatment with 50 mM 2-DG (n = 5 independent experiments per group). (g) Immunoblot of ATGL in the HEK293T cells 6 h after serum withdrawal (n = 10 independent experiments per group). (h, i) Immunoblot of ATGL in the HEK293T cells 6 h after treatment with amino acid or FAs free medium (n = 7 independent experiments per group). (j) Immunoblot of ATGL in the WCE and LD fraction extracted from HepG2 cells 6 h after glucose withdrawal. Three times

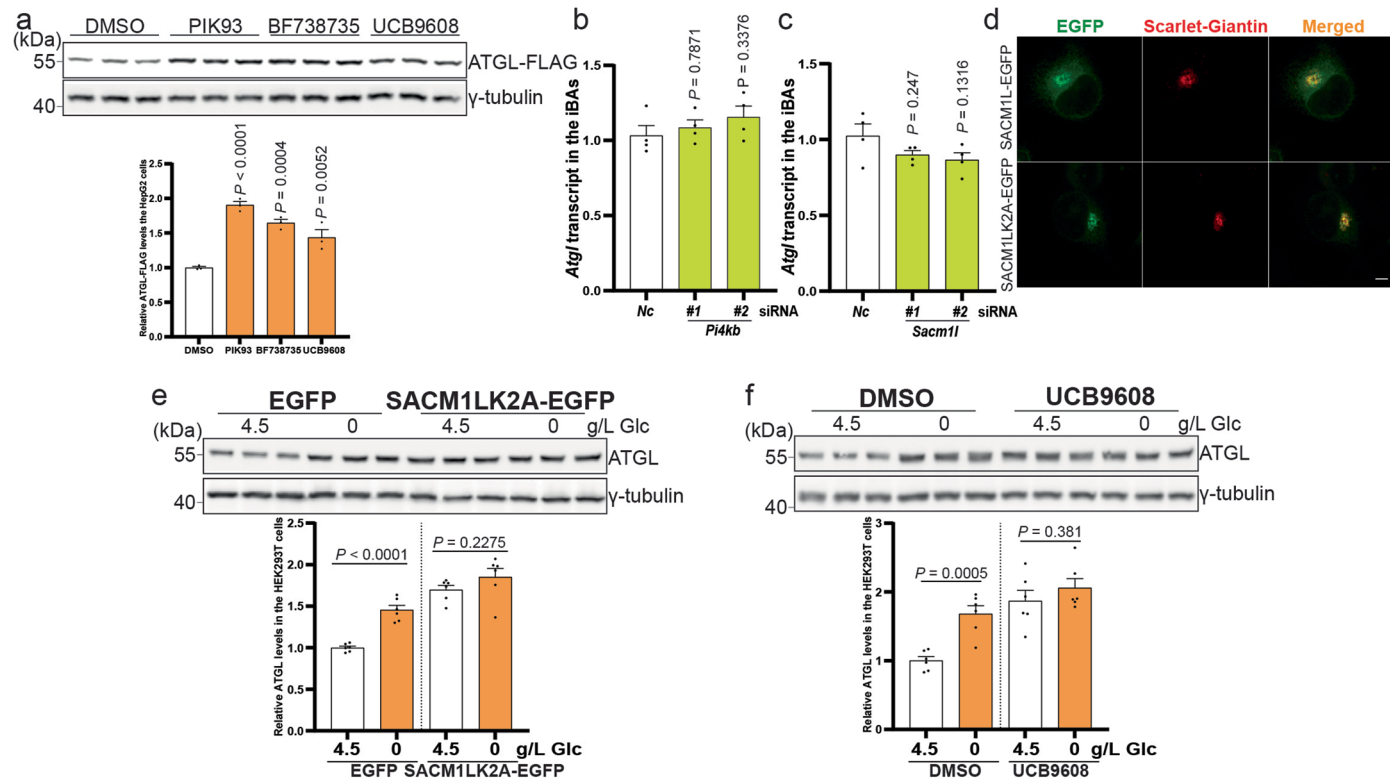
repeated independently with similar results. (k) Representative images of LDs in the HepG2 cells 48h after treatment with DGAT1/2 inhibitors and stained by BODIPY. Scale bar, 5 μ m. Two times repeated independently with similar results. (l, m) Immunoblot of ATGL in the HepG2 cells 6 h after glucose withdrawal or 2-DG treatment in the absence of LDs (n = 4 independent experiments per group). (n) Representative images of Golgi in the HepG2 cells treated with BFA and immunostained with anti-GM130. Scale bar, 20 μ m. Two times repeated independently with similar results. (o, p) Immunoblot of ATGL in the HepG2 cells 6 h after glucose withdrawal or 2-DG treatment in the absence of Golgi (n = 4 independent experiments per group). Results are shown as mean \pm s.e.m. and analyzed using two-tailed unpaired *t*-test (a to i, l, m, o (DMSO) and p) and two-tailed Mann-Whitney test (o (BFA)). Source numerical data and unprocessed blots are available in source data.



Extended Data Fig. 4 | See next page for caption.

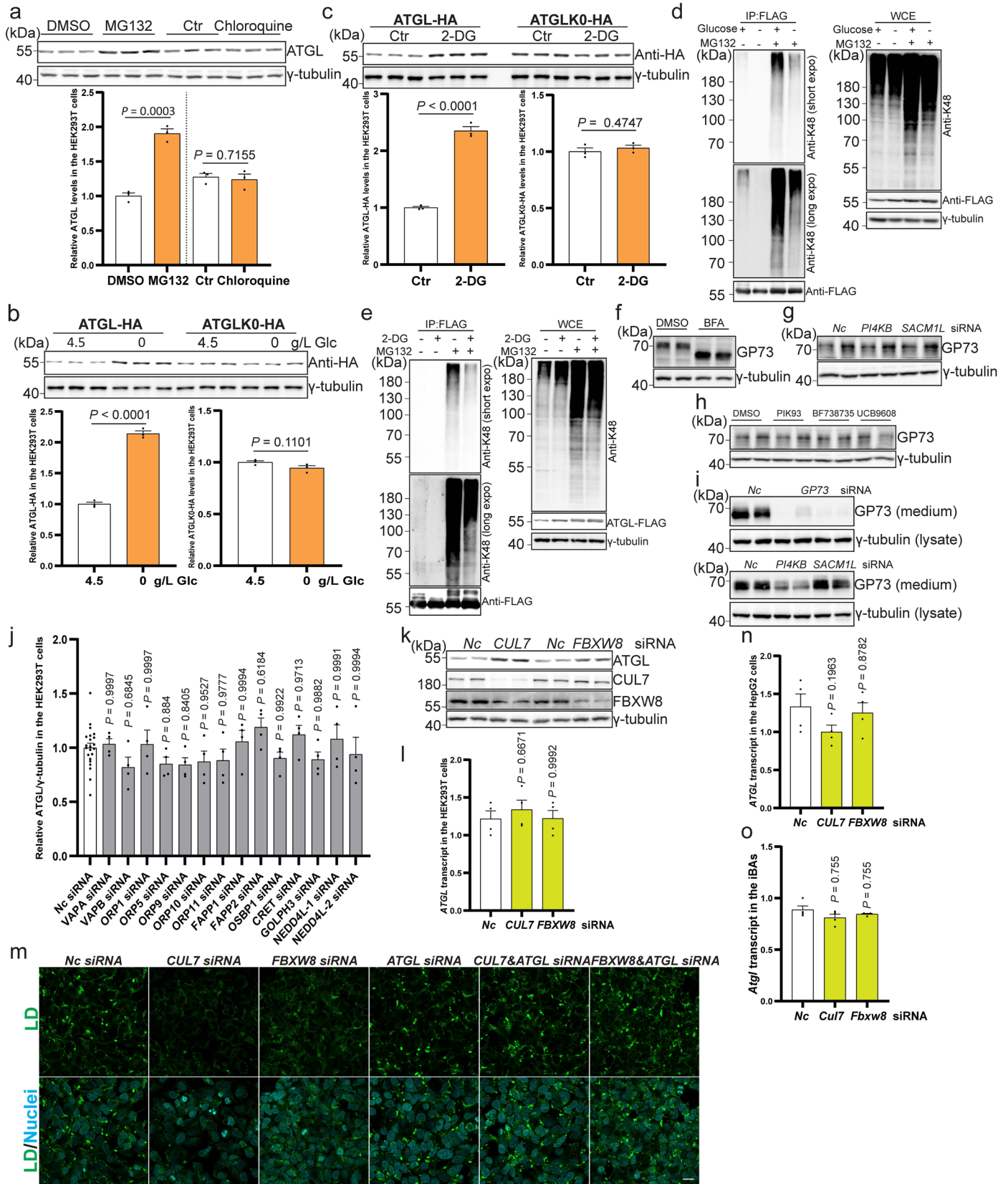
Extended Data Fig. 4 | Golgi PtdIns4P regulates ATGL protein stability in the Golgi apparatus. (a) Representative images of P4M-EGFP signal in the HEK293-AAV cells 12 h after glucose deprivation (n = 107 cells per group). Scale bar, 5 μ m. (b) Representative images of SACMIL-EGFP signal in the HEK293-AAV cells after glucose deprivation. Scale bar, 5 μ m. Three times repeated independently with similar results. (c) Determination of total PtdIns4P levels in the HEK293T cells 24 h after glucose deprivation (n = 9 independent experiments per group). (d) Immunoblot of ATGL and pAMPK in the HEK293T cells after treatment with AMPK inhibitor Compound C (Cpd C) and activator AICAR (n = 4 independent experiments per group). (e) PtdIns4P quantification via immunostaining in the HEK293-AAV cells after treatment with Cpd C and AICAR (n = 67 cells per group). Scale bar, 5 μ m. (f–g) Quantification of PtdIns4P levels and Golgi area via immunostaining in the HEK293-AAV cells 72 h after *PI4KB* and *SACMIL* knockdown (n = 103 cells per group in f; n = 130 cells per group in g). Scale bar,

5 μ m. (h) Quantification of *ATGL* transcript in the HEK293T cells 72 h after *PI4KB* and *SACMIL* knockdown (n = 4 independent experiments per group). (i–j) Quantification of PtdIns4P levels and Golgi area via immunostaining in the HEK293-AAV cells after 24 h treatment with 5 μ M PIK93, 10 μ M BF738735 and 10 μ M UCB9608 (n = 136 cells per group in i; n = 100 cells per group in j). Scale bar, 5 μ m. (k) Immunoblot of ectopically expressed ATGL in the HEK293T cells 24 h after treatment with 5 μ M PIK93, 10 μ M BF738735 and 10 μ M UCB9608 (n = 3 independent experiments per group). Results are shown as mean \pm s.e.m. and analyzed using two-tailed unpaired *t*-test (c and d (Ctr and AICAR)), two-tailed Mann-Whitney test (a, d (DMSO and Cpd C) and e), one-way ANOVA method with Dunnett correction for multiple comparisons between control and other groups (h and k) and Kruskal-Wallis test with Dunn's correction for multiple comparisons between control and other groups (f, g, i and j). Source numerical data and unprocessed blots are available in source data.



Extended Data Fig. 5 | Glucose deprivation elevates ATGL protein in the Golgi via PtdIns4P regulation. (a) Immunoblot of ectopically expressed ATGL in the HepG2 cells 24 h after treatment with 5 μ M PIK93, 10 μ M BF738735 and 10 μ M UCB9608 (n = 3 independent experiments per group). (b) Quantification of *Atgl* transcript levels in the iBAs 72 h after *Pi4kb* knockdown (n = 4 independent experiments per group). (c) Quantification of *Atgl* transcript levels in the iBAs 72 h after *Sacm1* knockdown (n = 4 independent experiments per group). (d) Representative images of SACM1L-EGFP and SACM1LK2A-EGFP in the HEK293-AAV cells. Scale bar, 5 μ m. Two times repeated independently with similar results.

(e) Immunoblot of ATGL in the HEK293T cells 6 h after treatment with glucose free medium under the background of SACM1LK2A-EGFP overexpression (n = 6 independent experiments per group). (f) Immunoblot of ATGL in the HEK293T cells 6 h after glucose deprivation under the background of UCB9608 treatment (n = 6 independent experiments per group). Results are shown as mean \pm s.e.m. and analyzed using two-tailed unpaired *t*-test (e and f) and one-way ANOVA method with Dunnett correction for multiple comparisons between control and other groups (a to c). Source numerical data and unprocessed blots are available in source data.

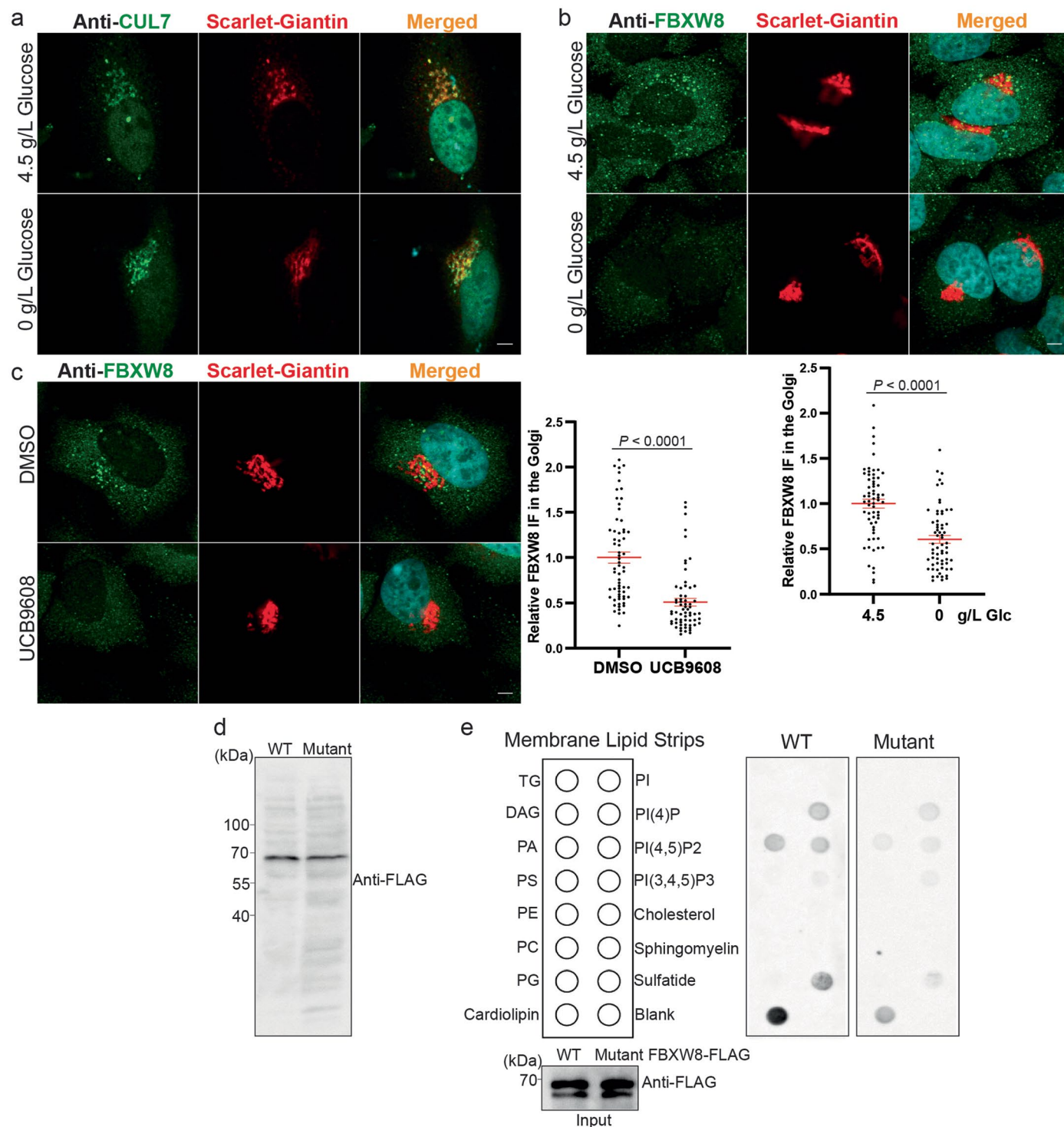


Extended Data Fig. 6 | See next page for caption.

Extended Data Fig. 6 | Glucose deprivation decreases ATGL poly-ubiquitylation via Golgi resident E3 ligase complex CUL7FBXW8.

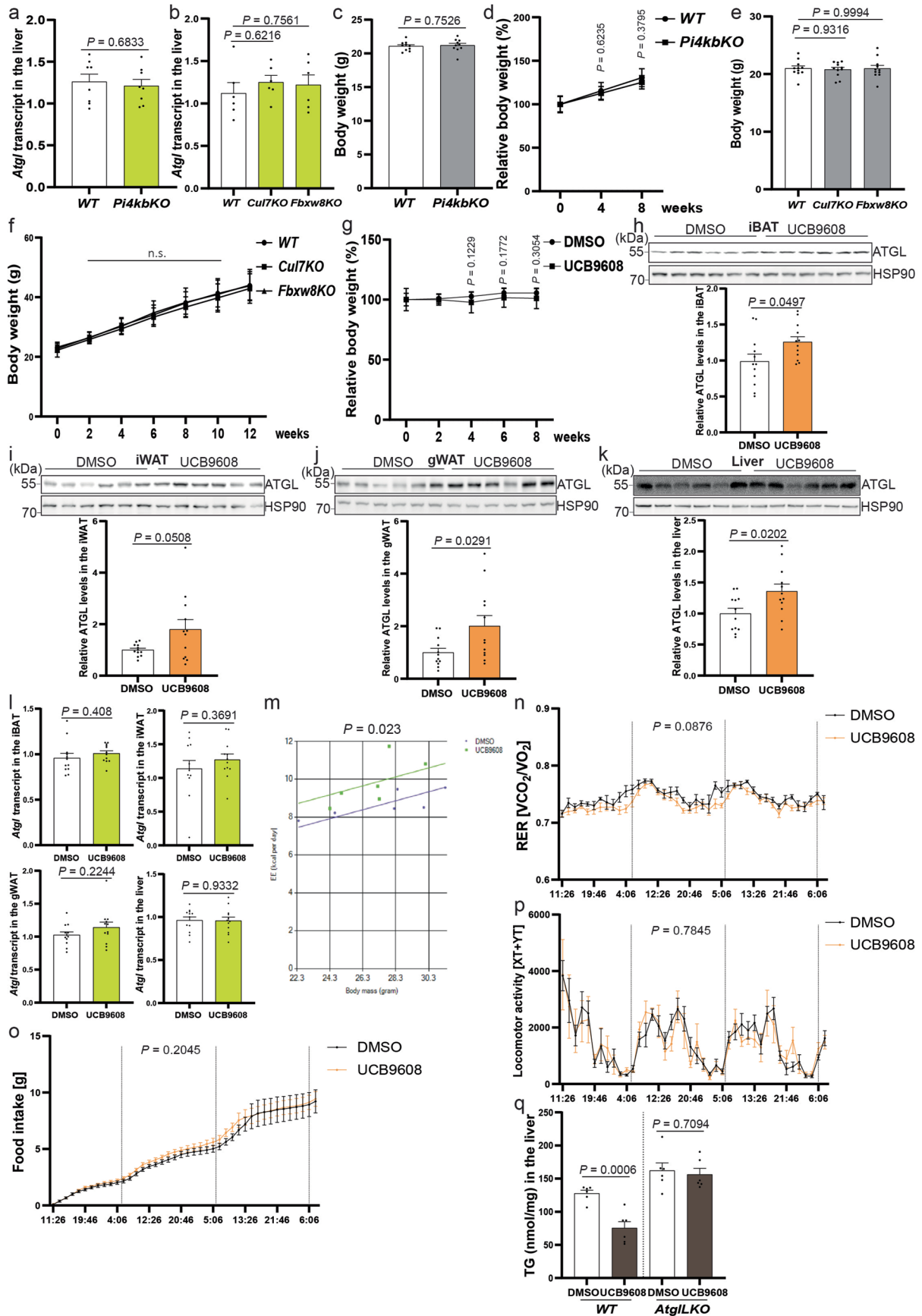
(a) Immunoblot of ATGL in the HEK293T cells 12 h after treatment with 10 μ M MGL32 and 100 μ M Chloroquine (n = 3 independent experiments per group). (b, c) Immunoblot of ATGL-HA and ATGLK0-HA in the HEK293T cells after glucose withdrawal or 50 mM 2-DG treatment (n = 3 independent experiments per group). (d, e) K48-linkage polyubiquitylation pattern detection of HEK293T cells transfected by ATGL-FLAG and treated with glucose-free medium or 2-DG, followed by IP to enrich ATGL-FLAG. Three times repeated independently with similar results. (f, i) Immunoblot of GP73 in the WCE or secreted GP73 in the medium of HEK293-AAV cells after treatment with 5 μ g/mL BFA, 5 μ M PIK93, 10 μ M BF738735, 10 μ M UCB9608 or different siRNAs. Two times repeated independently with similar results. (j) Quantification of ATGL protein levels of HEK293T WCE in a small-scale siRNA screen via immunoblot (n = 22 or 4 independent experiments for control or other groups). (k) Immunoblot of ATGL

in the HEK293T cells 72 h after *CUL7* and *FBXW8* knockdown. Four times repeated independently with similar results. (l) Quantification of *ATGL* transcript levels in the HEK293T cells 72 h after *CUL7* and *FBXW8* knockdown (n = 4 independent experiments per group). (m) Representative images of LDs stained via BODIPY in the HEK293-AAV cells 72 h after siRNA knockdown in the presence of 200 μ M oleic acid. Scale bar, 20 μ m. Three times repeated independently with similar results. (n) Quantification of *ATGL* transcript levels in the HepG2 cells 72 h after *CUL7* and *FBXW8* knockdown (n = 4 independent experiments per group). (o) Quantification of *Atgl* transcript levels in the iBAs 72 h after *Cul7* and *Fbxw8* knockdown (n = 4 independent experiments per group). Results are shown as mean \pm s.e.m. and analyzed using two-tailed unpaired *t*-test (a to c), one-way ANOVA method with Dunnett correction for multiple comparisons between control and other groups (j, l and n) and Kruskal-Wallis test with Dunn's correction for multiple comparisons between control and other groups (o). Source numerical data and unprocessed blots are available in source data.



Extended Data Fig. 7 | Recruitment of FBXW8 to the Golgi via interaction with PtdIns4P. (a) Representative immunofluorescent images of endogenous CUL7 in the HEK293-AAV cells after treatment with glucose free medium. Scale bar, 5 μ m. Three times repeated independently with similar results. (b) Representative immunofluorescent images of endogenous FBXW8 in the HEK293-AAV cells after treatment with glucose free medium ($n = 64$ cells per group). Scale bar, 5 μ m. (c) Representative immunofluorescent images of endogenous FBXW8 in the HEK293-AAV cells after treatment with UCB9608

($n = 64$ cells per group). Scale bar, 5 μ m. (d) Immunoblot of ectopically expressed protein in the HEK293T cells stably expressing FBXW8-FLAG and FBXW8 mutant-FLAG. Two times repeated independently with similar results. (e) Blotting analysis of Membrane Lipid Strips incubated with purified recombinant protein FBXW8-FLAG and FBXW8 mutant-FLAG. Three times repeated independently with similar results. Results are shown as mean \pm s.e.m. and analyzed using two-tailed unpaired t -test (b) and two-tailed Mann-Whitney test (c). Source numerical data and unprocessed blots are available in source data.

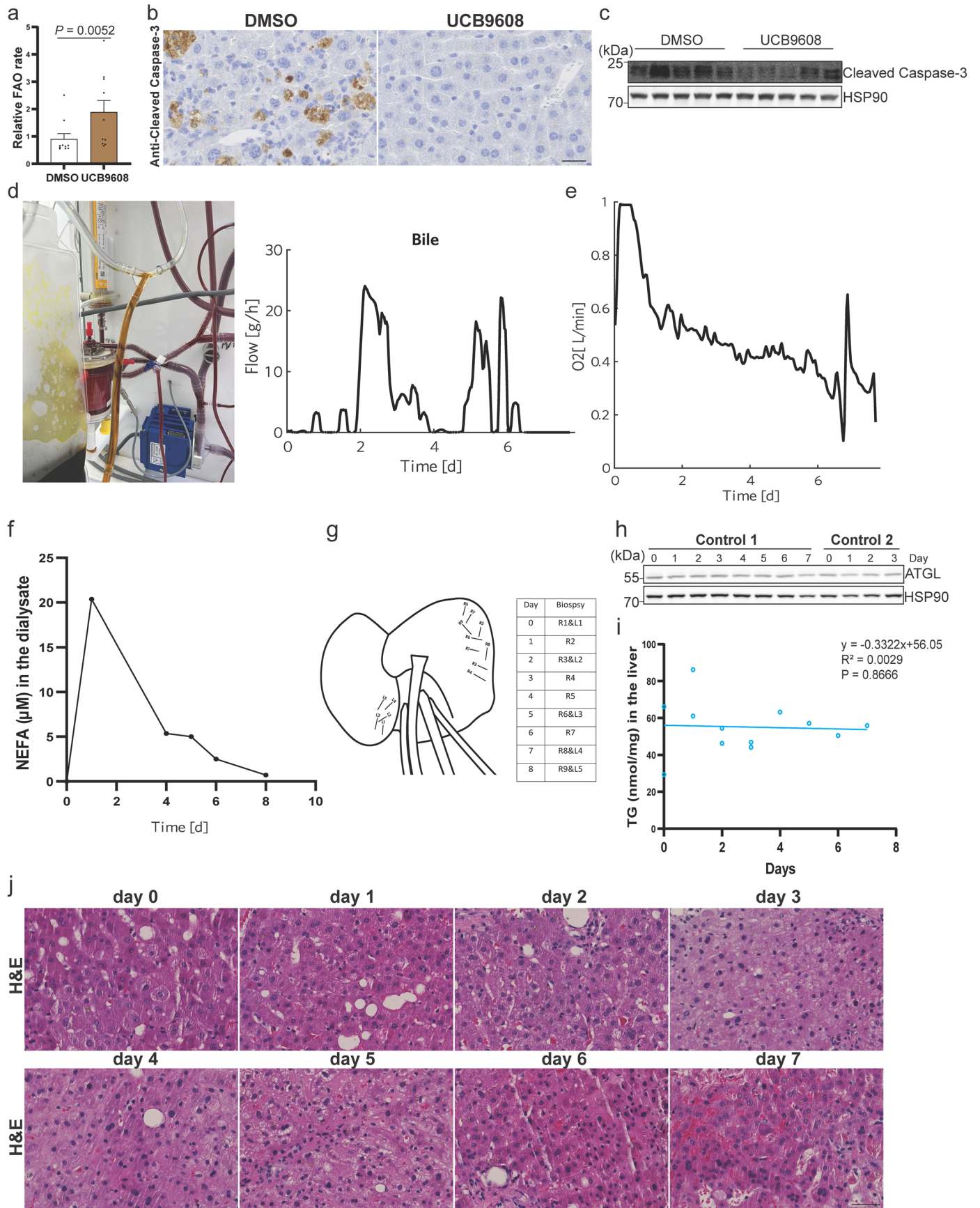


Extended Data Fig. 8 | See next page for caption.

Extended Data Fig. 8 | Regulation of ATGL-driven lipolysis and fatty liver development via manipulating Golgi PtdIns4P- CUL7FBXW8-ATGL axis.

(a) Quantification of *Atgl* transcript levels in the liver from hepatocyte specific *Pi4kb* knockout mice (n = 8 mice per group). (b) Quantification of *Atgl* transcript in the liver from hepatocyte specific *Cul7* and *Fbxw8* knockout mice (n = 6 mice per group). (c) Body weight of hepatocyte specific *Pi4kb* knockout mice fed in NCD 4 weeks after AAV8 administration (n = 10 mice per group). (d) Body weight of hepatocyte specific *Pi4kb* knockout mice fed in HFD 8 weeks after AAV8 administration (n = 5 mice per group). (e) Body weight of hepatocyte specific *Cul7* and *Fbxw8* knockout mice fed in NCD 4 weeks after AAV8 administration (n = 11 mice per group). (f) Body weight of hepatocyte specific *Cul7* and *Fbxw8* knockout mice fed in HFD 12 weeks after AAV8 administration (n = 9 mice per group). (g) Body weight gain during the period of UCB9608 treatment (n = 10 mice per group). (h–k) Immunoblot of ATGL protein in the adipose depots and

liver from DMSO- and UCB9608-treated mice (n = 12 mice per group). (l) Quantification of *Atgl* transcript levels in the adipose depots and liver from DMSO- and UCB9608-treated mice via qPCR (n = 12 mice per group). (m–p) Energy expenditure, Respiratory Exchange Ratio (RER), Food intake and Locomotor activity measurement of wild-type mice after 3 weeks administration of UCB9608 via HFD (n = 6 mice per group). (q) Hepatic TG levels in DMSO- and UCB9608-treated wild-type (*WT*) and liver specific *Atgl* knockout (*Atgl^{LLKO}*) mice (n = 6 mice per group). Results are shown as mean ± s.e.m. (except d, f and g shown as mean ± s.d.) and analyzed using two-tailed unpaired *t*-test (a, c, d, g (4 and 6 weeks), h to l, and q), two-tailed Mann-Whitney test (g (8 weeks)), ANCOVA (m), one-way ANOVA method with Dunnett correction for multiple comparisons between control and other groups (b, e and f) and two-way ANOVA method (n-p). Source numerical data and unprocessed blots are available in source data.



Extended Data Fig. 9 | See next page for caption.

Extended Data Fig. 9 | Amelioration of murine MASH progression and steatosis in human liver graft via blocking Golgi PtdIns4P generation.

(a) Measurement of liver fatty acid oxidation using ^{14}C -palmitate as the substrate (n = 10 mice per group). (b) Immunohistological analyses of liver apoptosis in the MASH mice via cleaved Caspase-3 antibody. Scale bar, 25 μm . Representative images from 10 mice per group with similar results. (c) Immunoblot of cleaved Caspase-3 in the adipose tissue from MASH mice. Two times repeated independently with similar results. (d) Bile acid excretion from the liver graft during 8 days of perfusion. (e) Oxygen consumption rate of the liver graft treated with UCB9608 over the course of perfusion. One liver graft used for perfusion.

(f) Measurement of NEFA levels in the dialysate. Three times repeated technically with similar results. (g) Time points and locations of punch biopsies from the liver graft. (h, i) Immunoblot of ATGL protein and quantification of TG levels in the human liver biopsies taken at different time points from control grafts. Three times repeated technically with similar results. (j) H&E stainings of biopsies taken at different time points. Scale bar, 50 μm . One liver piece at every time point. Data were presented as mean \pm s.e.m. and analyzed using two-tailed Mann-Whitney test (a) and two-tailed Pearson's correlation (i). Source numerical data and unprocessed blots are available in source data.

Reporting Summary

Nature Research wishes to improve the reproducibility of the work that we publish. This form provides structure for consistency and transparency in reporting. For further information on Nature Research policies, see our [Editorial Policies](#) and the [Editorial Policy Checklist](#).

Statistics

For all statistical analyses, confirm that the following items are present in the figure legend, table legend, main text, or Methods section.

n/a Confirmed

- The exact sample size (n) for each experimental group/condition, given as a discrete number and unit of measurement
- A statement on whether measurements were taken from distinct samples or whether the same sample was measured repeatedly
- The statistical test(s) used AND whether they are one- or two-sided
Only common tests should be described solely by name; describe more complex techniques in the Methods section.
- A description of all covariates tested
- A description of any assumptions or corrections, such as tests of normality and adjustment for multiple comparisons
- A full description of the statistical parameters including central tendency (e.g. means) or other basic estimates (e.g. regression coefficient) AND variation (e.g. standard deviation) or associated estimates of uncertainty (e.g. confidence intervals)
- For null hypothesis testing, the test statistic (e.g. F , t , r) with confidence intervals, effect sizes, degrees of freedom and P value noted
Give P values as exact values whenever suitable.
- For Bayesian analysis, information on the choice of priors and Markov chain Monte Carlo settings
- For hierarchical and complex designs, identification of the appropriate level for tests and full reporting of outcomes
- Estimates of effect sizes (e.g. Cohen's d , Pearson's r), indicating how they were calculated

Our web collection on [statistics for biologists](#) contains articles on many of the points above.

Software and code

Policy information about [availability of computer code](#)

Data collection

Data analysis

For manuscripts utilizing custom algorithms or software that are central to the research but not yet described in published literature, software must be made available to editors and reviewers. We strongly encourage code deposition in a community repository (e.g. GitHub). See the Nature Research [guidelines for submitting code & software](#) for further information.

Data

Policy information about [availability of data](#)

All manuscripts must include a [data availability statement](#). This statement should provide the following information, where applicable:

- Accession codes, unique identifiers, or web links for publicly available datasets
- A list of figures that have associated raw data
- A description of any restrictions on data availability

Field-specific reporting

Please select the one below that is the best fit for your research. If you are not sure, read the appropriate sections before making your selection.

Life sciences Behavioural & social sciences Ecological, evolutionary & environmental sciences

For a reference copy of the document with all sections, see [nature.com/documents/nr-reporting-summary-flat.pdf](https://www.nature.com/documents/nr-reporting-summary-flat.pdf)

Life sciences study design

All studies must disclose on these points even when the disclosure is negative.

Sample size	Sample sizes were determined on the basis of previous experiments in our lab and common standard in the metabolism field using similar methods (ref 18, 20).
Data exclusions	No samples were excluded from any analyses.
Replication	Experimental findings were verified by biological replicates and technical replicates, each experiment was performed multiple times as indicated in the figure legends.
Randomization	All experiments were randomized
Blinding	The investigators were not blinded to the mice as they themselves were treating and sacrificing the mice. However, the investigators were blinded for sample processing.

Reporting for specific materials, systems and methods

We require information from authors about some types of materials, experimental systems and methods used in many studies. Here, indicate whether each material, system or method listed is relevant to your study. If you are not sure if a list item applies to your research, read the appropriate section before selecting a response.

Materials & experimental systems

n/a	Involved in the study
<input type="checkbox"/>	<input checked="" type="checkbox"/> Antibodies
<input type="checkbox"/>	<input checked="" type="checkbox"/> Eukaryotic cell lines
<input checked="" type="checkbox"/>	<input type="checkbox"/> Palaeontology and archaeology
<input type="checkbox"/>	<input checked="" type="checkbox"/> Animals and other organisms
<input type="checkbox"/>	<input checked="" type="checkbox"/> Human research participants
<input checked="" type="checkbox"/>	<input type="checkbox"/> Clinical data
<input checked="" type="checkbox"/>	<input type="checkbox"/> Dual use research of concern

Methods

n/a	Involved in the study
<input checked="" type="checkbox"/>	<input type="checkbox"/> ChIP-seq
<input checked="" type="checkbox"/>	<input type="checkbox"/> Flow cytometry
<input checked="" type="checkbox"/>	<input type="checkbox"/> MRI-based neuroimaging

Antibodies

Antibodies used	ATGL (1:1000, Cell Signaling:2138S), CGI-58 (1:1000, Proteintech:12201-1-AP), phosphor-HSL(Ser660) (1:1000, Cell Signaling:45804S), PLIN1 (1:1000, Cell Signaling:9349S), HSL (1:1000, Cell Signaling:4107S), γ -tubulin (1:10000, Sigma:T6557), FLAG (1:10000, Sigma:F3165; 1:1000, Cell Signaling:2368S and 8146S), MGL (1:1000, Abcam:ab77398), AKT (1:1000, Cell signaling:9272), Phospho-AKT(1:1000, Cell Signaling:4060), CUL7 (1:1000, Santa Cruz:sc-53810), HSP90 (1:1000, Cell Signaling:4877S), K48 linkage specific ubiquitin antibody (1:1000, Cell Signaling:33959), HA (1:1000, Cell signaling:3724S), FBXW8 (1:1000, Santa Cruz:sc-514385; 1:1000, Sigma:HPA038851), PI4KB antibody (1:1000, Sigma:HPA006280), SACM1L(1:1000, Sigma:HPA069869), PtdIns4P (1:100, Echelon Biosciences:Z-P004), TGN46 (1:1000, Abcam:ab2809), PLIN2 (1:1000, Abcam:ab108323), GP73 (1:1000, Sigma:HPA011929), MAOA (1:1000, Abcam:ab126751), PMP70 (1:10000, Sigma:SAB4200181), Calnexin (1:1000, Cell signaling:2433S), ARF1 (1:1000, Invitrogen:PA1-127), RAB7 (1:1000, Cell Signaling:9367T), Na+/K+ ATPase (1:1000, Abcam:ab7671), GAPDH (1:10000, Cell Signaling:2118S), cleaved Caspase-3 (1:1000, Cell Signaling:9661), HRP-conjugated anti-rabbit IgG (1:10000, Cell signaling: 7074), HRP-conjugated anti-mouse IgG (1:10000, Cell signaling:7076), Anti-Rabbit IgG (H+L) Cross-Adsorbed Secondary Antibody, Alexa Fluor 488 (1:200, Thermo:A21206), Anti-Rabbit IgG (H+L) Cross-Adsorbed Secondary Antibody, Alexa Fluor 568 (1:200, Thermo:A11042), Anti-Mouse IgG (H+L) Highly Cross-Adsorbed Secondary Antibody, Alexa Fluor 488 (1:200, Thermo:A11029)
Validation	We validated ATGL,PI4KB, SACM1L, CUL7, FBXW8 and GP73 antibodies in both mouse and human cell lines for WB application via siRNA knockdown. The following antibodies were validated by previous publication or commercial companies: Anti-CGI-58 for WB of mouse sample (DOI: 10.1074/jbc.RA120.014682), anti-pHSL for WB of mouse sample (DOI: 10.1038/s42255-021-00489-2), anti-PLIN1 for WB of mouse sample (10.1172/jci.insight.139160), anti-HSL for WB of mouse sample (https://www.cellsignal.com/products/primary-antibodies/hsl-antibody/4107), anti- γ -tubulin for WB of mouse and human sample (https://www.sigmaaldrich.com/CH/de/product/sigma/t6557), anti-FLAG for WB (DOI: 10.1038/s42255-021-00489-2), anti-FLAG for immunostaining (https://www.cellsignal.com/products/primary-antibodies/dykdddk-tag-9a3-mouse-mab-binds-to-same-epitope)

as-sigma-aldrich-anti-flag-m2-antibody/8146), anti-MGL for WB of mouse sample (DOI: 10.3892/etm.2021.11004), anti-AKT for WB of mouse sample (<https://www.nature.com/articles/s41467-023-39715-8>), anti-phospho-AKT for WB of mouse sample (<https://www.nature.com/articles/s41467-023-39715-8>), anti-HSP90 for WB of human and mouse sample (<https://www.nature.com/articles/s41467-023-39715-8>), anti-K48 ubi for WB of human sample (DOI: 10.1038/s42255-021-00489-2), anti-HA for WB (10.1038/s41467-021-24097-6), anti-PtdIns4P for IF of human cells (<https://doi.org/10.1083/jcb.201905162>), anti-PLIN2 for WB of human samples (<https://www.abcam.com/products/primary-antibodies/rabbit-monoclonal-epr3713-to-perilipin-2-ab108323.html>), anti-MAOA for WB of human samples (<https://www.abcam.com/products/primary-antibodies/monoamine-oxidase-amao-a-antibody-epr7101-ab126751.html>), anti-PMP70 for WB of human sample (DOI: 10.1038/s42255-021-00489-2), anti-Calnexin for WB of human sample (<https://www.cellsignal.com/products/primary-antibodies/calnexin-antibody/2433>), anti-ARF1 for WB of human sample (<https://www.thermofisher.com/antibody/product/ARF1-Antibody-Polyclonal/PA1-127>), anti-RAB7 for WB of human sample (<https://www.cellsignal.com/products/primary-antibodies/rab7-d95f2-xp-rabbit-mab/9367>), anti-Na⁺/K⁺ ATPase for WB of human sample (<https://www.abcam.com/products/primary-antibodies/alpha-1-sodium-potassium-atpase-antibody-4646-ab7671.html>), anti-GAPDH for WB of human sample (<https://www.cellsignal.com/products/primary-antibodies/gapdh-14c10-rabbit-mab/2118>), anti-cleaved Caspase-3 for WB of mouse sample (<https://www.cellsignal.com/products/primary-antibodies/cleaved-caspase-3-asp175-antibody/9661>)

Eukaryotic cell lines

Policy information about [cell lines](#)

Cell line source(s)	293-AAV and 293-LTV cell lines were purchased from Cell Biolabs Inc. (cat. AAV-100; LTV-100); HEK293T cell line was purchased from abcam. iBAs cells were previously established by Ronald Kahn lab as indicated in manuscript. HepG2 cells were purchased from ATCC.
Authentication	293-AAV and 293-LTV cells were not authenticated, however the AAV and LV produced from these cells were titred by PCR. iBA cells were previously validate by gene expression and functional assay (OCR). HepG2 cells and HEK293T cells were validated via PCR.
Mycoplasma contamination	The cells were regularly tested, all cell lines tested were negative for mycoplasma contamination.
Commonly misidentified lines (See ICLAC register)	No commonly misidentified cell lines were used in the study.

Animals and other organisms

Policy information about [studies involving animals](#); [ARRIVE guidelines](#) recommended for reporting animal research

Laboratory animals	C57Bl/6 male mice were used. Both male and female mice of B6J.129(B6N)-Gt(ROSA)26Sortm1(CAG-cas9*,-EGFP)Fezh/J strain and male mice of Atgl floxed strain were used. All the experiments were started when mice were 8 to 10 weeks of age. Mice were kept on an inverted 12-h:12-h dark:light cycle and fed ad libitum with a chow diet or high fat diet, at 40% humidity and 22 degree.
Wild animals	No wild animals were used in the study.
Field-collected samples	No field-collected samples were used in the study.
Ethics oversight	All animal experiments were approved by the Veterinary office of the Canton of Zurich and Institutional Animal Care and Use Committee of Sun Yat-sen University

Note that full information on the approval of the study protocol must also be provided in the manuscript.

Human research participants

Policy information about [studies involving human research participants](#)

Population characteristics	24 middle-aged lean-to-obese sedentary men (age 35.5 ± 1.5 years, BMI 28.9 ± 1.1 kg.m ⁻² , adiposity 25.7 ± 1.6%) with different degree of insulin sensitivity.
Recruitment	The participants included in the study were recruited as part of a larger clinical study previously described in Balaz et al., 2014 (https://doi.org/10.1002/oby.20764). Patients with chronic disease or regular use of pharmacotherapy were not eligible to participate. All patients underwent complex metabolic phenotyping, including assessment of insulin sensitivity by Euglycemic hyperinsulinemic clamp (EHC) and abdominal subcutaneous adipose tissue biopsy both at fasted state, as well as during the steady state of EHC. 24 individuals with sufficient amount of adipose tissue samples were randomly selected for this study without any selection bias, and based on their insulin sensitivity index (M value) assigned to insulin sensitive (n=16, M value 0.14 ± 0.02 mg/kg BW/min/insulin μU/ml) and insulin resistant (n=8, M value 0.04 ± 0.01 mg/kg BW/min/insulin μU/ml) subgroups. All study participants provided witnessed written informed consent before entering the study.
Ethics oversight	The EHC study was approved by the by the Local Ethics Committee (Bratislava, Slovakia) and conforms to the ethical guidelines of the 2000 Helsinki declaration. The human liver grafts were perfused after being discarded from all Swiss transplant centers. Use of discarded grafts was approved by local authorities (Kantonale Ethik Kommission Zürich KEK Nr. 2017-000412).

Note that full information on the approval of the study protocol must also be provided in the manuscript.